École Polytechnique Fédérale de Lausanne

Nonlinear activation function for analog neurons in low power deep learning applications

by Eliot Abramo

Professor: Prof. Romain Fleury

Supervisor: PhD. Tim Tuuva

Abstract

This report explores the implementation of physical nonlinearities as activation functions in analog neural networks. It aims to address the high power demands of digital deep learning systems. Two experimental approaches are investigated.

The first utilizes a binary tunable phase metasurface, based on coupled resonators controlled by PIN diodes, to modulate microwave reflections in a passive, low-power manner.

The second approach investigates the optical emulation of the Gaussian Error Linear Unit (GELU) activation function. It uses structured incoherent light and Fresnel transmission principles.

Together, these methods demonstrate the feasibility of embedding physical nonlinearities into analog computing architectures, offering a pathway to energy-efficient deep learning systems.

Contents

1 Introduction

Neural networks are at the heart of Artificial Intelligence (AI). They reflect the brain's decision-making processes [1] and consist of a hierarchy of interconnected nodes (or artificial neurons) through which information flows from input to output. Each node computes a weighted sum of its inputs and passes the result through an activation function to determine whether to activate and propagate the signal forward. The output layer then produces the network's final decision or classification [2], [3].

Central to this is the nonlinear activation function. Without it, neural networks would function as simple linear regression models, lacking the capacity to learn complex patterns and relationships. Hence, making them considerably less attractive for deep learning applications [4].

Digital neural networks, while effective, are inherently power hungry, especially when scaled to the levels required by modern Artificial Intelligence. Thus forcing big data companies, such as Google and Microsoft, to invest in nuclear power plants for the sole purpose of powering the next waves of AI innovation [5], [6]. This creates a pressing need for an alternative approach that can deliver the necessary computing power with greater energy efficiency.

This report investigates the implementation of physical nonlinearities to enable low-power activation functions in analog neural networks, addressing the research question: **Nonlinear activation function for analog neurons in low power deep learning**. By leveraging the intrinsic nonlinear behaviors of physical systems, it is conceivable to achieve the desired activation functions with lower energy consumption. We explore two distinct physical mechanisms to achieve this.

The first approach focuses on the development and testing of a **binary tunable metasurface**. This metasurface utilizes coupled resonators capable of switching the phase shift of reflected electromagnetic waves between discrete states (0 and π).

The second approach explores the optical equivalent of the Gaussian Error Linear Unit (GELU) activation function. This method leverages the physical principles of Fresnel equation and wave propagation.

2 Tunable binary phase Metasurface

2.1 Objectives

The objective of the metasurface project is to develop and characterize a binary tunable metasurface. Ambient electromagnetic interference (EMI) from sources such as WiFi routers will serve as an input to the microwave cavity. Such a system would be passive by definition and therefore shouldn't be power demanding. This initiative builds upon the papers "*Shaping complex microwave fields in reverberating media with binary tunable metasurfaces*"[7] as well as "*Hybridized resonances to design tunable binary phase metasurface unit cells*"[8], which demonstrate a viable design for such a system.

Other objectives of this project are to conduct detailed simulations of the metasurface to validate the design and ensure its theoretical feasibility. A key constraint is manufacturability: the design must be compatible with standard Printed Circuit Board (PCB) fabrication tolerances and use dielectrics within the range of materials commonly available to manufacturers[1]. Once the design is finalized, a prototype of a single unit cell will be assembled and characterized using a vector network analyzer (VNA) to verify alignment with simulation results.

Subsequently, sufficient unit-cells will be assembled to create a phased array antenna that will then be integrated into a microwave cavity. Within this cavity, the performance of the phased antenna array will be characterized using a VNA.

A key deliverable of the project will be a complete, well-documented framework—including all supporting code and methodologies—to enable future researchers to replicate and build upon this work.

[1] A PCB is a combination of layers of dielectric material and a conductor. Our design for the metamaterial follows the same basic topology, hence we can see how it would correlate to do this if only as a cost saving measure and to allow rapid prototyping.

2.2 Background

In this section, a detailed theoretical grounding will be done to explain all aspects encountered during the development of this project.

2.2.1 Proposed Unit Cell

The underlying geometrical configuration is inspired by prior works [7], [8] as seen in Fig. (1).

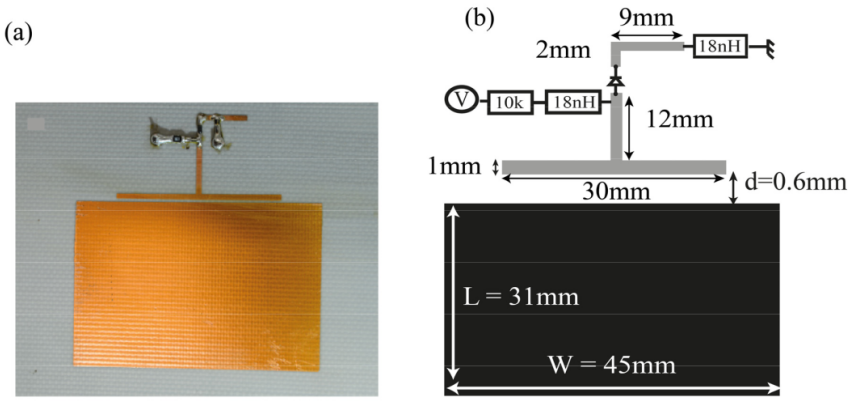

Figure 1: Original unit cell design [8]

A key modification involves shifting the operational frequency from a single, fixed point at 2466 MHz to a broader target bandwidth of 2427–2447 MHz. This bandwidth was chosen as in the laboratory where the experiment is taking place, Channel 6 of the WiFi band is the strongest[2] (c.f Fig. 2).

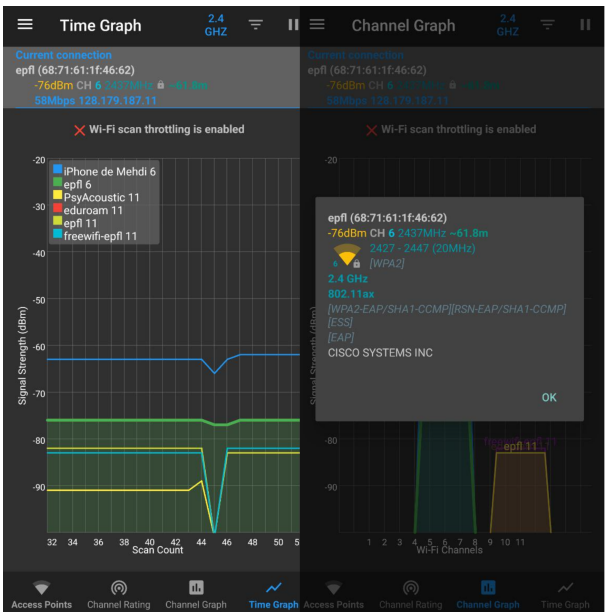

Figure 2: WiFi Analyzer result in laboratory to choose operating frequency

[2]Found using a standard WiFi Analyzer application [9]

The objective of the new surface is to be able to function with a minimum of a 60 MHz bandwidth instead of a single fixed frequency. This bandwidth was calculated to allow for standard PCB manufacturer fabrication tolerances. By designing for a broader band in which the desired π phase shift occurs approximately, rather than at an exact frequency, the system gains robustness.

We will see in later sections how, with these modifications, most geometrical aspects of the unit cell will change.

Additionally, the choice of dielectric material is revised to align with standard PCB fabrication capabilities, as the NELTEC NH9338ST used in earlier studies is not readily available or manufacturable.

2.2.2 Dielectric loss vs lossless : FR4 vs ROGERS

The choice of dielectric material is important as its dielectric constant, ε, governs signal propagation characteristics, while the loss tangent, $\tan\delta$, dictates the dissipation [10].

Initial simulations were conducted using lossless materials to validate the geometrical parameters of the unit cell as the inclusion of losses introduces additional complexities. Once the geometry was confirmed, the transition to lossy materials was expected to result in predictable differences in attenuation levels, which are discussed in detail in this corresponding background chapter.

Let us consider the propagation of an electromagnetic wave in a homogeneous, isotropic, dielectric material. From Helmholtz equation we have that:

$$\nabla \times \nabla \times E = w^2 \mu \cdot \varepsilon \cdot E = \frac{w^2}{c^2} \mu_0 \cdot \varepsilon(w) \cdot E \tag{1}$$

whose solutions are given by[3] $E(r,t) = E(r)e^{-jwt}$.

The complex permittivity $\varepsilon(w)$ of a dielectric material (denoted ε so forth for simplicity) is expressed as:

$$\varepsilon = \varepsilon' - j\varepsilon'' \tag{2}$$

where ε' represents the energy storage capability and ε'' the energy loss per cycle. The loss tangent $\tan\delta$ is defined as the ratio of the imaginary to real components:

$$\tan\delta = \frac{\varepsilon''}{\varepsilon'} \tag{3}$$

The power dissipated per unit volume in the dielectric is given by:

$$P_{loss} = \frac{1}{2} \cdot w \cdot \varepsilon'' \cdot |E|^2 = \frac{1}{2} \cdot w \cdot \varepsilon' \cdot \tan\delta \cdot |E|^2 \tag{4}$$

where ω is the angular frequency and $|E|$ is the magnitude of the electric field. This equation quantifies how materials with higher $\tan\delta$ will dissipate more energy, reducing the effective Q-factor of the resonator in question.

[3]The convention j for the imaginary unit was chosen to avoid confusion with current. Such convention is applied to the whole paper

The propagation of electromagnetic waves in lossy dielectric media can be described by the complex propagation constant

$$\gamma = \alpha + j\beta \tag{5}$$

where α is the attenuation constant and β is the phase constant.

For low-loss dielectrics ($\tan\delta \ll 1$), the attenuation constant is approximated as:

$$\alpha \approx \frac{w\sqrt{\mu\varepsilon'}}{2} \cdot \tan\delta \tag{6}$$

indicating that even small $\tan\delta$ values can cause significant attenuation at GHz frequencies due to their linear dependence on frequency and field strength.

For example, at $f = 2.4$ GHz we can compare two different materials: Rogers RO4350B and FR4[4]. With Rogers RO4350B ($\varepsilon_r' \approx 3.66$, $\tan\delta \approx 0.0031$) and FR4 ($\varepsilon_r' \approx 4.5$, $\tan\delta \approx 0.02$) [11], [12], and assuming $\mu = \mu_0$, the ratio of attenuation constants is:

$$\frac{\alpha_{FR4}}{\alpha_{Rogers}} = \frac{\sqrt{\varepsilon_{FR4}}\tan\delta_{FR4}}{\sqrt{\varepsilon_{Rogers}}\tan\delta_{Rogers}} = \frac{\sqrt{4.5}\cdot 0.02}{\sqrt{3.66}\cdot 0.0031} \approx 7.2$$

showing that, at 2.4 GHz, given $\tan\delta$ and ε, FR4 is estimated to introduce $\sim 7\times$ more dielectric loss than RO4350B under identical conditions. This underscores the need for low-loss dielectrics in applications requiring sharp spectral features and minimal insertion loss.

The quality factor Q of a metasurface resonance is defined as:

$$Q = \frac{w_0}{\Delta w} \tag{7}$$

where ω_0 is the resonance frequency and $\Delta\omega$ is the full width at half maximum (FWHM) of the resonance. The dielectric losses contribute to broadening $\Delta\omega$, thus reducing Q. The overall Q of a resonant metasurface element can be approximated by:

$$\frac{1}{Q} = \frac{1}{Q_{rad}} + \frac{1}{Q_{dielectric}} + \frac{1}{Q_{conductor}} \tag{8}$$

where $Q_{dielectric}$ accounts for material losses and is inversely proportional to $\tan\delta$, Q_{rad} accounts for radiative losses and $Q_{conductor}$ ohmic losses.

Thus, selecting low-loss dielectrics like Rogers (low $\tan\delta$) over FR4 directly enhances the Q-factor, enabling sharper resonances, improved spectral selectivity, and reduced insertion losses, all critical for high-performance RF metasurface applications.

From a theoretical perspective, the use of lossless dielectrics ($\tan\delta \to 0$) leads to an ideal metasurface response characterized by minimal insertion loss.

[4]choice is not coincidental, corresponds to analysis made to choose which dielectric will be used in the metasurface

However, practical materials inevitably introduce some loss, and the design challenge lies in optimizing the geometry and material composition to mitigate its effects. The use of low-loss substrates can sustain high-Q resonances.[13]

High-loss materials introduce power dissipation and signal attenuation, degrading the metasurface's resonance quality and efficiency. In contrast, low-loss materials enable sharp resonance features, high field enhancement, and low insertion loss.[13]

An important consequence of introducing dielectric losses is the emergence of new attenuation features in the transmission spectrum. In lossless materials, $\varepsilon'' = 0$, the propagation constant is purely real for propagating modes resulting in no material absorption and sharp resonances determined solely by geometry, c.f. Section 2.2.3. However, when dielectric losses are present, $\varepsilon'' > 0$, the propagation constant acquires an imaginary component, β (c.f Eq. 5).

The frequency dependence of ε'', and therefore $\tan\delta$, means that attenuation is not uniform across all frequencies. Near natural resonances, the energy density stored is higher, causing stronger interaction with the dielectric and leading to localized 'hot spots' of energy dissipation. This results in new attenuation peaks, frequency ranges where transmission drops sharply due to enhanced dielectric losses, even in regions that would otherwise support high transmission in the lossless case.

Moreover, in periodic metasurfaces, electromagnetic waves satisfy Bloch-Floquet conditions, and the allowed modes are determined by the periodic structure and dielectric function. Losses introduce complex terms into the dispersion relation:

$$\det|\mathbf{M}(w, k_B) - I| = 0, \tag{9}$$

where $\mathbf{M}$ is the transfer matrix of the unit cell. In the presence of losses, the Bloch wavevector becomes complex:

$$k_B = k'_B - jk''_B, \tag{10}$$

with k''_B representing the exponential decay of the wave amplitude along the propagation direction [14]. This leads to the formation of attenuation bands, frequency regions where wave propagation is suppressed due to dielectric loss, effectively creating loss-induced stopbands that are absent in the lossless case.

Therefore we can see how the introduction of dielectric losses transforms the metasurface electromagnetic behavior. It doesn't simply broaden existing resonances, but also introduces new attenuation features in the transmission spectrum. These effects highlight the importance of low-loss dielectric materials and precise geometric design in ensuring high-quality, high-efficiency metasurface performance.

2.2.3 Geometric sensitivity

The geometric design of the metasurface is also directly tied to its performance and characteristics. This dependence is because the physical dimensions of the resonant elements are comparable to the wavelength of incident waves, leading to strong field localization and enhanced sensitivity to dimensional variations [13].

When a resonator's geometry changes, whether through variation in trace width, gap dimension, or substrate thickness, it changes the distributed inductance (L) and capacitance (C) of the system. This is important as the resonance frequency f_0 can be expressed as:

$$f_0 \approx \frac{1}{2\pi\sqrt{LC}} \tag{11}$$

Therefore, even subtle geometric changes introduce nonlinear shifts in f_0. From Eq. 7 we can see how this impacts the Q-factor and overall resonance behavior. Quantitatively, we can find the impact of a relative change in inductance or capacitance on a relative shift in frequency by doing a sensitivity analysis of Eq. 11. First we take the natural logarithm to simplify the expression:

$$f_0 = \frac{1}{2\pi\sqrt{LC}} \leftrightarrow ln(f_0) = ln(\frac{1}{2\pi}) - \frac{1}{2}ln(LC) \tag{12}$$

Therefore we can clearly see that:

$$\frac{\Delta f_0}{f_0} = -\frac{1}{2}\left(\frac{\Delta L}{L} + \frac{\Delta C}{C}\right) \tag{13}$$

For example, consider a lossless microstrip line[5] with $\frac{w}{h} \geq 1$. The inductance and capacitance can be found using:

$$L = \frac{120\pi l}{v_0} \cdot \left[\frac{w}{h} + 1.393 + 0.667\ln\left(\frac{w}{h} + 1.444\right)\right]^{-1} \tag{14}$$

$$C = \frac{\varepsilon_r l}{120\pi v_0} \cdot \left[\frac{w}{h} + 1.393 + 0.667\ln\left(\frac{w}{h} + 1.444\right)\right] \tag{15}$$

with w the trace width, h the dielectric thickness, l the trace length, ε_r the relative permittivity, and v_0 the speed of light in vacuum. Using the main reflector patch of the reference unit cell as an example:

$$w = 45.000\text{mm}, \quad h = 2.000\text{mm}, \quad l = 31.000\text{mm}, \quad \varepsilon_r = 4.5, \quad v_0 = 3 \times 10^8\text{m/s},$$

We find that $L = 1.499$nH, $C = 32.11$pF. Therefore, using Eq. 11: $f_0 \approx 725.44$MHz.

Suppose we apply a 1% reduction to these dimensions[6].

We find that $L_{new} = 1.484$nH, $C_{new} = 31.78$pF.

Hence, $\Delta L = -1.5 \cdot 10^{-11}$ and $\Delta C = -3.3 \cdot 10^{-13}$.

[5] Microstrip line used as an example as it closely resembles the structure of the metasurface we are designing.

[6] Which is coherent with standard manufacturing tolerances.

Now we can use Eq. 13 to see how it impacts the resonance frequency:

$$\frac{\Delta f_0}{f_0} = -\frac{1}{2}\left(\frac{\Delta L}{L} + \frac{\Delta C}{C}\right) = 0.0101 \implies \Delta f_0 = 7.36\text{MHz},$$

Whilst this change in resonant frequency may seem small, Eq. 7 shows that it directly affects the quality factor, and thus the sharpness of the resonance. This highlights how even small geometric variations can directly impact the system's performance.

At these frequencies, the Bethe small-hole coupling model and Babinet's principle provide additional theoretical foundations [15], [16]. The Bethe-Bouwkamp theory shows that the coupling through sub-wavelength apertures scales with the cube of the aperture diameter, d^3, making them extremely sensitive to small dimensional changes. Similarly, Babinet's principle relates the electromagnetic response of complementary structures, indicating that geometric perturbations in one structure are mirrored in its complement.

Perturbation theory of electromagnetic resonators provides a rigorous foundation for understanding this sensitivity. It predicts that a perturbation in permittivity $\delta\varepsilon(\mathbf{r})$ or permeability $\delta\mu(\mathbf{r})$ leads to a first-order shift in resonance frequency given by:

$$\frac{\Delta\omega}{\omega} \approx -\frac{1}{2}\frac{\int_V (\delta\varepsilon(\mathbf{r})|\mathbf{E}|^2 + \delta\mu(\mathbf{r})|\mathbf{H}|^2)\, dV}{\int_V (\varepsilon|\mathbf{E}|^2 + \mu|\mathbf{H}|^2)\, dV} \tag{16}$$

where $\mathbf{E}$ and $\mathbf{H}$ are the unperturbed fields evaluated over the volume V of the resonator [17]. This expression reveals that localized field enhancements, prevalent in metamaterials due to strong confinement, amplify the impact of small geometric changes. Localized field enhancements mean that even minor deviations in material properties or geometry can lead to shifts in resonant frequency, affecting the device's performance.

For example, consider a unit cell where electric fields are concentrated across a narrow capacitive gap of width $w = 0.2\,\text{mm}$, over a volume $\Delta V = 1\,\text{mm}^3$. Assume that we are focusing on a localized perturbation and that due to fabrication tolerances, a trace edge shifts by $\Delta w = -0.05\,\text{mm}$. Since the local electric field in the gap scales approximately as $E \propto 1/w$, the energy density scales as $|E|^2 \propto 1/w^2$. Therefore:

$$\left(\frac{w}{w + \Delta w}\right)^2 = \left(\frac{0.2}{0.15}\right)^2 \approx 1.78.$$

Assuming the rest of the mode remains unchanged, and that the perturbed region originally had relative permittivity $\varepsilon_r = 3.66$ (RO4350B). The effective change in permittivity within that region is:

$$\delta\varepsilon(\mathbf{r}) = \varepsilon_0 \cdot \varepsilon_r \cdot (1.78 - 1) \approx 2.85 \cdot \varepsilon_0.$$

Substituting into Eq. 16:

$$\frac{\Delta\omega}{\omega} \approx -\frac{1}{2} \cdot \frac{2.85\varepsilon_0 \cdot |\mathbf{E}|^2 \cdot \Delta V}{\varepsilon_0 \cdot |\mathbf{E}|^2 \cdot V_{\text{total}}} = -\frac{1}{2} \cdot \frac{2.85 \cdot \Delta V}{V_{\text{total}}}.$$

Now let's assume that the region affected by the geometry change occupies just 1% of the total volume where the field energy is concentrated. Then its contribution to the total mode energy is ($\frac{\Delta V}{V_{\text{total}}} = 0.01$) and we have that:

$$\frac{\Delta\omega}{\omega} \approx -\frac{1}{2} \cdot 0.0285 \approx -0.0143$$

This corresponds to a frequency shift of $\approx -1.43\%$, or $-34\,\text{MHz}$ at $2.4\,\text{GHz}$, arising purely from a $50\mu\text{m}$ geometric deviation.

This coupling of geometry and electromagnetic response shows that any deviation can ripple through to affect resonance frequency, bandwidth, and phase characteristics, altering key features of the unit cell.

2.2.4 Coupling of parasitic and reflector patch

The unit cell of the binary phase metasurface is based on the principle of hybridized resonant elements, where the coupling between a reflector patch and parasitic patch resonator is mediated by a PIN diode[7]. This diode functions as a tunable impedance and allows the coupling strength to be controlled depending on its bias.

When the system is forward biased, the diode bridges the resonators, resulting in strong coupling ($\kappa > 0$, where κ represents the coupling coefficient [18]), which leads to the hybridization of their modes and enables resonance at the operational frequency. In this state, the unit cell resonates, producing a π phase shift on the reflected wave.

In contrast, when reverse-biased, the diode acts as a high impedance and inhibits coupling between the patches ($\kappa \sim 0$). In this uncoupled state, the parasitic resonator operates independently from the main reflector, and the system exhibits minimal interaction at the design bandwidth. As a result, the eigen-frequencies of the system revert to the natural resonances of the individual elements and there is negligible phase shift in the reflected wave, rendering the unit cell effectively 'transparent'.

It is important to note that the "on" and "off" states are defined by convention. The one explained here, forward-biased is on and reverse-biased is off, is rooted in our choice of electronic control. Our choice contrasts the reference papers [7], [8] which work with a reverse logic, forward-biased represents a 0-state and reverse-biased a π-state.

[7] c.f Annex for theoretical grounding and justification for choice of PIN diode.

2.2.5 Coupling mechanisms and mode hybridization

To fully understand how this design facilitates phase modulation and resonance control, it is essential to examine the physical principles that govern coupling in this system. The Coupled Mode Theory (CMT) serves as a foundational framework to describe the coupling phenomena [19].

Building on the work of "*Analogy to Debye model in metamaterials: Resonant frequency shifting due to coupling*"[20] and their study of coupled metamaterial systems, it can be understood how coupling in our system works. This paper provides a theoretical reasoning to describe coupling mechanisms between resonant structures; specifically, they derive the CMT equation, Eq. 17, governing the temporal evolution of the modal amplitudes of two structures, $a_1(t)$ and $a_2(t)$, representing the localized field strengths in each resonator:

$$j\frac{d}{dt}\begin{bmatrix} a_1 \\ a_2 \end{bmatrix} = \begin{bmatrix} w_0 - j\gamma & g \\ g & w_0 - j\gamma \end{bmatrix} \tag{17}$$

Where g represents the strength of energy exchange between resonators, γ models intrinsic and radiative losses, and ω_0 is the uncoupled natural frequency of each resonator. The model energies are given by $|a_1|^2$ and $|a_2|^2$. Solving this eigenvalue problem in the lossless case first for simplicity, they obtain that:

$$w = w_0 \pm g \tag{18}$$

which corresponds to the eigenstate $\left[1, 1\right]^+$. Here, $\left[1, 1\right]^+$ represents the symmetric mode, where both coupled elements oscillate in-phase with equal amplitude.

In the extended system of multiple unit cells, coupling interactions accumulate and manifest as collective behaviors described by a tight-binding or Debye model analogy. Here, the system's Hamiltonian matrix takes the form:

$$H = \begin{bmatrix} \omega_0 & g & 0 & \cdots & 0 \\ g & \omega_0 & g & \cdots & 0 \\ 0 & g & \omega_0 & \cdots & 0 \\ \vdots & \vdots & \vdots & \ddots & g \\ 0 & 0 & 0 & g & \omega_0 \end{bmatrix} \tag{19}$$

which leads to the dispersion relation:

$$w(k) = w_0 \pm 2g \cdot \cos(kd) \tag{20}$$

where d is the lattice spacing and k the Bloch wavevector which describes the phase shift of waves propagating through a periodic structure, quantifying how the wave's phase evolves between adjacent unit cells.

This reveals that inter-cell coupling induces frequency shifts twice those of intra-cell coupling ($\omega_0 \pm 2g$ vs. $\omega_0 \pm g$), with the relation $g_{\text{intra}} = 2g_{\text{inter}}$. This will be useful when analyzing the experimental results.

Moreover, by controlling the coupling strength through the PIN diode bias, we can dynamically tune the metasurface's phase response and resonance behavior.

This tunability may be further enhanced by engineering slight asymmetries in the resonator design, which can introduce quasi-bound states in the continuum (quasi-BICs).

These modes, when realized, arise from destructive interference between resonant modes that would otherwise couple to free-space radiation, effectively trapping energy within the structure. As a result, these modes can exhibit high-Q resonances, characterized by sharp spectral features and reduced radiative loss.

The high-Q nature of such modes is essential for applications requiring strong field localization and spectral selectivity, such as phase modulation in our design. Unlike conventional PIT or EIT, where coupling occurs between bright and dark modes, quasi-BICs emerge from interference between nearly identical bright modes with minor structural differences, offering the potential for robust and sharp spectral control even in the presence of imperfections [21]–[23].

2.2.6 Chaotic Dynamics in a Microwave Cavity with Metasurface

The dynamics of electromagnetic fields within resonant cavities can exhibit either regular or chaotic behavior, depending on the geometry, boundary conditions and other factors.

Considering a system with a steel box microwave cavity containing a phased array antenna, chaotic behavior ensures isotropic mode mixing. Which reduces modal interference and standing wave formation. This allows the metasurface to respond more uniformly to the input wave (external EMI). Hence, it is interesting to determine if our system is indeed chaotic.[24]

To investigate chaos in our system, we first establish its mathematical foundation. The electromagnetic fields inside the cavity satisfy Maxwell's equations with boundary conditions imposed by the metallic walls and the metasurfaces. Expanding the fields as superpositions of cavity modes:

$$\mathbf{E}(\mathbf{r}, t) = \sum_n a_n(t) \cdot \mathbf{E}_n(\mathbf{r}) \tag{21}$$

$$\mathbf{H}(\mathbf{r}, t) = \sum_n b_n(t) \cdot \mathbf{H}_n(\mathbf{r}) \tag{22}$$

The system reduces to a set of coupled nonlinear ordinary differential equations (ODEs) for the mode amplitudes:

$$\frac{d^2 a_n}{dt^2} + \omega_n^2 a_n + \sum_{m,k} \alpha_{nmk} a_m a_k + \beta_n \frac{da_n}{dt} = F_n(t) \tag{23}$$

where ω_n are the natural frequencies of the cavity, α_{nmk} represent nonlinear coupling coefficients from the metasurfaces, β_n accounts for losses, and $F_n(t)$ describes the external forcing. More precisely, $F_n(t)$ is the projection of the external field (i.e. incoming wave) onto the mode profile $\mathbf{E}_n(\mathbf{r})$.

With the system clearly described, we can employ the Melnikov method to identify chaos. The Melnikov method detects chaotic behavior in weakly perturbed Hamiltonian systems by examining the behavior of saddle points and their associated manifolds [25].

A saddle point is an equilibrium of a dynamical system where the Jacobian matrix of the linearized system has eigenvalues with both positive and negative real parts. This means there are directions in which trajectories approach the point and others in which they diverge [26]. Such points can give rise to homoclinic orbits, trajectories that leave and return to the same saddle point. Fig. 3 provides a graphical interpretation of this.

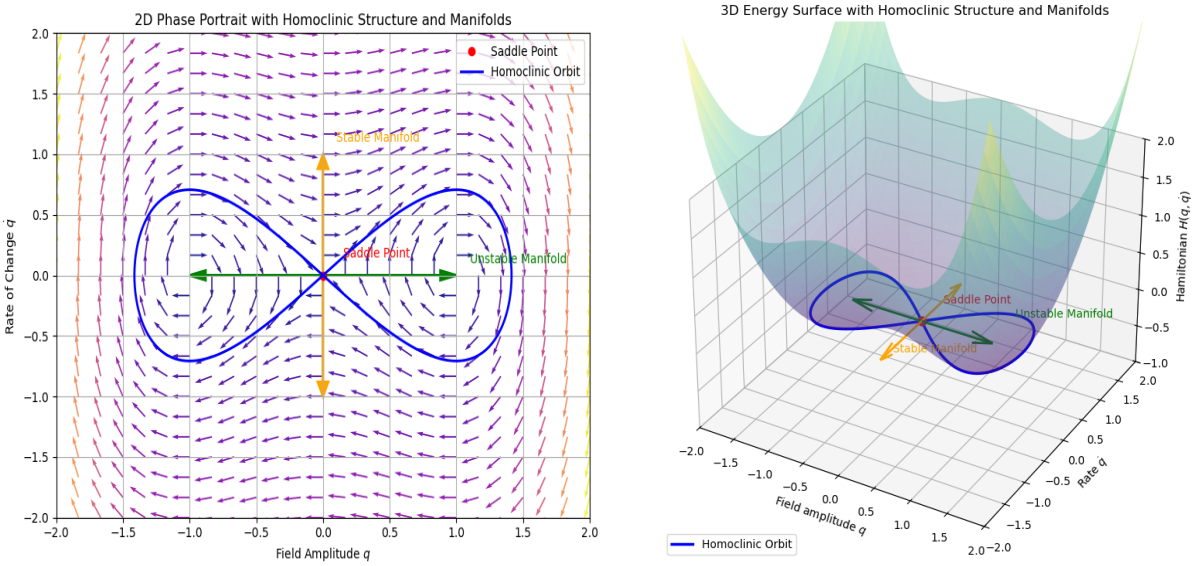

(a) 2D vector intuition

(b) 3D intuition

Figure 3: Graphical intuition for Saddle point and Homoclinc Orbit

To apply the Melnikov method, the following conditions must hold [25]:

1. The unperturbed system is Hamiltonian with a hyperbolic saddle and homoclinic orbit.

2. The perturbation is smooth, periodic and small.

3. The Melnikov integral converges.

We assume the cavity is Hamiltonian. This is justified because the unforced system is lossless and conservative[8] and we assume it supports discrete, well-defined modes in the absence of external excitation. In a simplified single-mode approximation, this unperturbed system reduces to:

$$\ddot{q} + \omega_0^2 q + \alpha q^3 = 0 \tag{24}$$

This corresponds to the potential:

$$U(q) = \frac{1}{2}\omega_0^2 q^2 + \frac{\alpha}{4} q^4 \tag{25}$$

Assuming $\alpha < 0$, the potential forms a double well with a local maximum at $q = 0$ and minima at $q = \pm\sqrt{-\frac{\omega_0^2}{\alpha}}$. The saddle point is at the origin.

[8]Lossless means there are no resistive or radiative energy losses; conservative means the total energy is preserved and the system can be described by a time-independent Hamiltonian.

Therefore, system admits a homoclinic orbit of the form [26]:

$$q_0(t) = A\,\mathrm{sech}(\lambda t) \tag{26}$$

with constants A, λ determined by ω_0 and α. This allows us to satisfy the first condition of the Melnikov Method.

For the second condition, we assume the metasurface introduces a time-dependent, cubic perturbation and that the external forcing is a harmonic source modeled by:

$$F_n(t) = F_0 \cos(\Omega t) \tag{27}$$

This is justified because 2.4GHz operation implies narrow-band harmonic content, and broadband excitation can be decomposed into Fourier modes. So cosine forcing captures the dominant term.

Therefore, the total perturbation takes the form[9]:

$$V(q,t) = -q\cos(\Omega t) \tag{28}$$

And the full Hamiltonian becomes:

$$H(q,p,t) = H_0(q,p) + \epsilon V(q,t) = H_0(q,p) + \epsilon \cdot F_0 \cdot q \cdot \cos(\Omega t) \tag{29}$$

where H_0 is the integrable unperturbed cavity, and $\epsilon \ll 1$ sets the perturbation strength. We assume H_0 is integrable, which is valid since we assume the unforced cavity supports discrete, regular modes with known solutions. Therefore, the perturbation is smooth, periodic in time and small amplitude, satisfying the second condition.

Finally, for the third condition, we evaluate the Melnikov integral along the separatrix orbit, which in this context refers to a homoclinic orbit. For the unperturbed system, this orbit is given by:

$$M(t_0) = \epsilon \int_{-\infty}^{\infty} V(q_0(t), t + t_0)\, dt = -\epsilon F_0 \int_{-\infty}^{\infty} q_0(t)\cos(\Omega(t + t_0))dt \tag{30}$$

We know that $\mathrm{sech}(\lambda t) = \frac{2}{e^{\lambda t} + e^{-\lambda t}}$. If we take the limit $|t| \to \infty$, we get that:

$$\mathrm{sech}(\lambda t) \approx 2e^{-\lambda|t|} \tag{31}$$

Therefore, for large t:

$$q_0(t) \approx 2Ae^{-\lambda|t|} \tag{32}$$

Meaning that the homoclinic orbit decays exponentially away from the saddle point. Ensuring convergence of Eq. 30. Hence, all three conditions are satisfied.

Moreover, seeing that Eq. 30 is periodic in t_0, it has simple zeros. This indicates transverse intersections of stable and unstable manifolds.

[9]We model the perturbation as $V(q,t) = -q\cos(\Omega t)$ so that the resulting equation of motion includes an additive forcing term $\cos(\Omega t)$. This represents a harmonic external field linearly coupled to the system, consistent with a narrowband excitation at frequency Ω.

We now state the formal result that connects transverse homoclinic intersections to chaos:

> **Theorem 3.4.3 (Smale–Birkhoff Homoclinic Theorem)** [25]: *Let a smooth area-preserving map have a transversal homoclinic point to a hyperbolic fixed point. Then the map has a compact invariant set on which the dynamics are topologically conjugate to a Bernoulli shift on two symbols.*

Unraveling this whole theorem is beyond the scope of this report, the key takeaway is that a single transverse intersection between stable and unstable manifolds is sufficient to guarantee chaotic dynamics. In our system, this is shown by zeros Eq 30, which signal such intersections. These imply the presence of symbolic dynamics, infinitely many unstable periodic orbits, and sensitive dependence on initial conditions.

As a representative case, consider a cavity resonating at $f_0 = 2.4\,\mathrm{GHz}$, giving $\omega_0 = 2\pi \cdot 2.4 \times 10^9\,\mathrm{rad/s}$, and let the nonlinearity coefficient be $\alpha = -10^{18}\,\mathrm{s}^{-2}$. Then:

$$q_0(t) \approx 0.1\,\mathrm{sech}(10^9 t),$$

and the Melnikov function evaluates to a sinusoid in t_0 with zero crossings spaced at $2\pi/\omega_0$. These crossings confirm the existence of transverse intersections required by the Smale–Birkhoff theorem.

Putting all of this together, we conclude that the Melnikov method shows that even minimal nonlinear structure in an RF cavity can compromise the integrable structure and introduce homoclinic tangles and symbolic dynamics. We can clearly conclude that our system is chaotic.

The presence of chaotic dynamics within the cavity has important implications for the performance of the phased array antenna. Chaos ensures a more uniform and isotropic field distribution, mitigating the formation of standing wave patterns that could bias the array's response. This leads to improved impedance matching, broader operational bandwidth, and reduced coupling between elements[27]. In chaotic cavities, the field distribution becomes more ergodic, which can reduce localized standing waves and improve average coupling uniformity.

2.3 Simulations

In this chapter, we present a detailed analysis of the simulation results for the tunable binary phase metasurface introduced in the theoretical framework. The objective is to validate the theoretical principles governing the system's behavior. The simulation studies cover the response of the metasurface to variations in frequency, geometrical parameters, and material properties, integrating the insights of coupling dynamics, hybridization, and cavity perturbations.

Before analyzing the frequency response, it is essential to outline the simulation setup used to model the metasurface. The full 3D geometry of the structure is shown in Fig. 4 and Fig. 5. Simulations were performed under idealized conditions, assuming a wave propagates toward the metasurface, reflects, and returns directly along its path. Hence, it wasn't necessary to include the cavity in the simulations. The meshing strategy employs high-frequency-adapted tetrahedral elements to ensure accurate resolution of the resonant features of the design. The PIN diode is represented as two lumped elements as seen in Fig. 6[10]

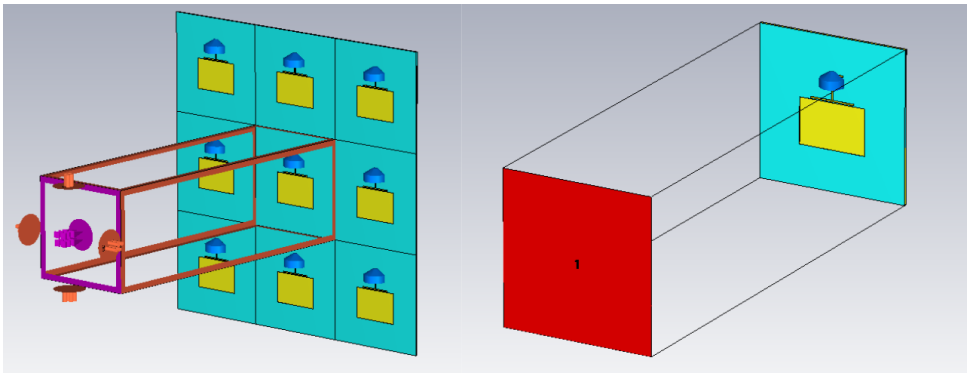

Figure 4: Representation of boundary conditions setup (left) and single unit cell (right)

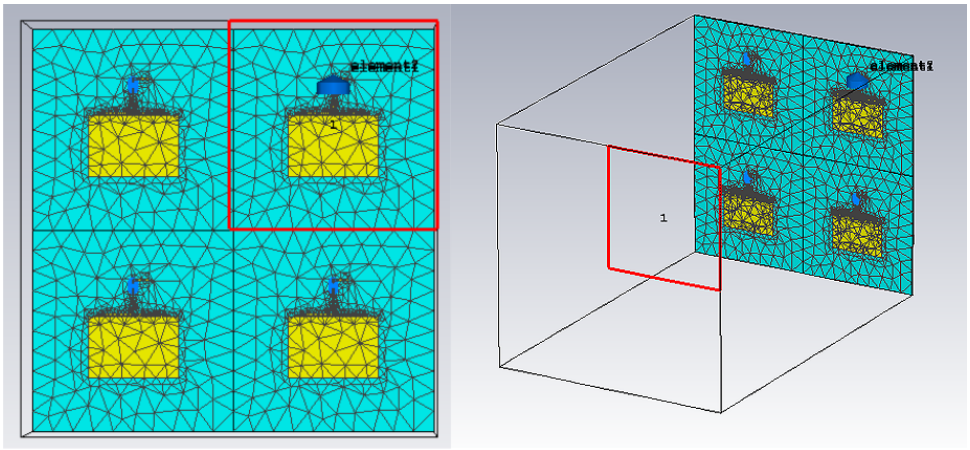

Figure 5: Representation of meshing strategy of metasurface

[10]c.f. Annex for details as to why a PIN diode can be reduced to two lumped elements.

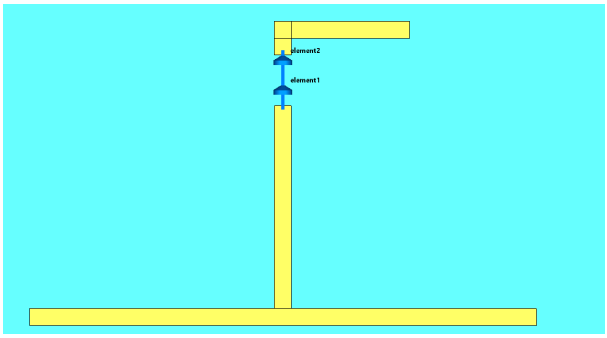

Figure 6: Representation of PIN diode as lumped element

We begin by examining the Smith chart representation of the reflection coefficient S_{11} seen in Fig. 7. The plotted trajectories for both the "on" (PIN diode forward biased) and "off" (PIN diode reverse biased) states reveal the change in impedance as a function of frequency.

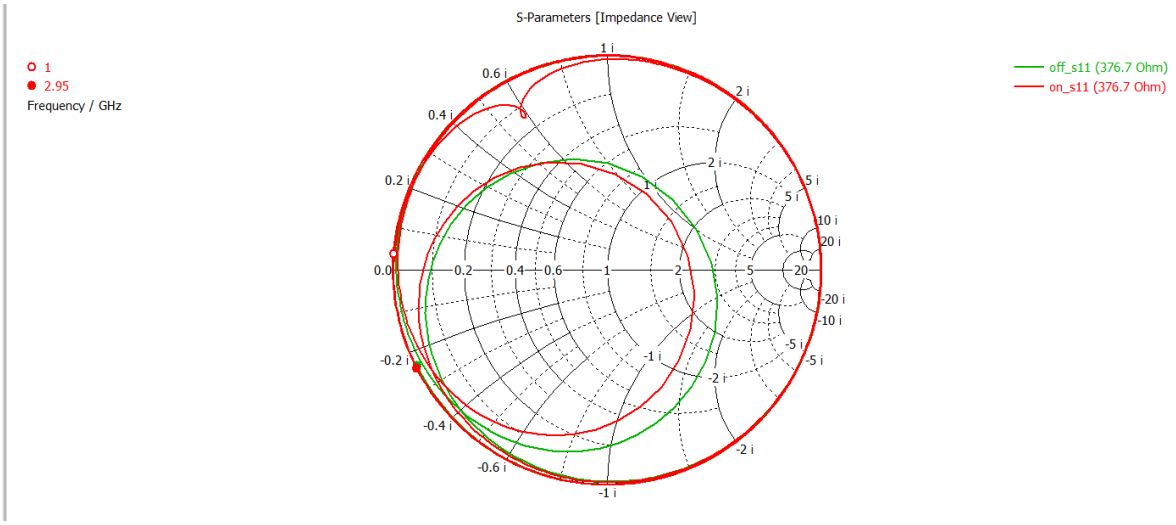

Figure 7: Smith chart representation of S_{11} for the metasurface.

The looping paths observed correspond to the evolution of the complex impedance as the frequency sweeps across the operational band. These results directly reflect the theory of hybridized resonances, where the coupling between the resonant elements in the metasurface leads to distinct impedance states. The shift of the resonant frequency and the marked separation between the states are consistent with the coupled mode theory equations discussed previously (Eq. 17). In particular, the observed impedance transition correlates with the control of the coupling coefficient κ, which governs the hybridization strength and thus modulates the reflection phase and magnitude (c.f Section 2.2.4).

The phase response seem in Fig. 8 provides further evidence of the metasurface's tunability.

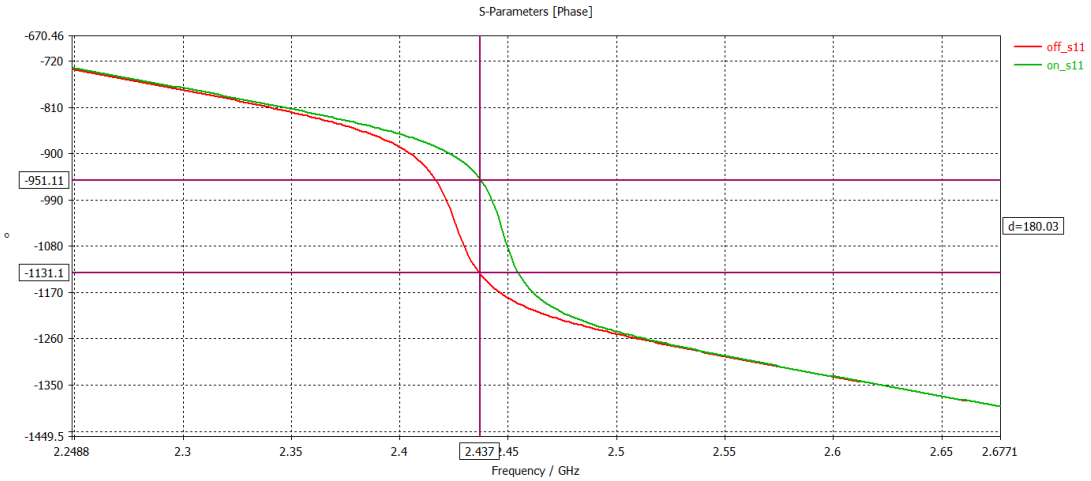

Figure 8: Phase response of S_{11} showing phase shift with frequency.

At 2.437 GHz, which corresponds to approximately the middle of the bandwidth identified in Section 2.1, a sharp phase shift of nearly 180.03° is observed. Which demonstrates the binary nature of the phase modulation. This behavior aligns with the prediction that strong coupling, facilitated by the forward bias of the PIN diode, enables a phase shift through hybridization of the resonant modes (c.f Section 2.2.4). The steepness of the phase transition can be calculated to be 8.89MHz/deg (off) and 10.51MHz/deg (on). This is indicative of the high-Q resonance associated with the chosen low-loss dielectric material. Hence, supporting the theoretical framework which emphasized the importance of dielectric loss tangent in sustaining sharp resonance features (c.f Section 2.2.2).

The magnitude response of S_{11}, depicted in Fig. 9, shows a pronounced dip at the resonance frequency, with ~ -8.6dB "on" state compared to the ~ -7dB "off" state.

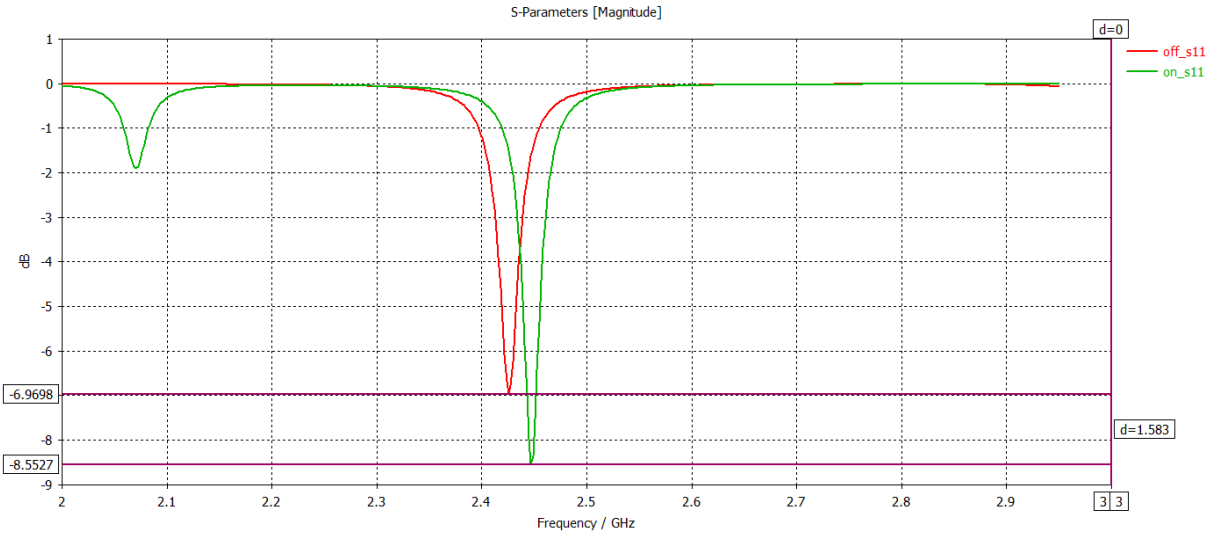

Figure 9: Magnitude response of S_{11} (in dB) highlighting the resonance dip.

This observation confirms that the forward bias of the diode enhances the coupling strength, leading to stronger hybridization and a higher amplitude resonance. The 1.6dB difference is a manifestation of reduced reflected power, consistent with the energy coupling into the resonant structure. This is in direct agreement with the expressions derived for Q-factors and insertion losses (c.f Eq. 4 and Eq. 8) in the Section 2.2.2, where low-loss dielectrics enable narrower and more selective resonances.

A closer inspection of the real and imaginary components of S_{11}, seen in Fig. 10, elucidates the resonance behavior further. The real part exhibits characteristic peaks and valleys, while the imaginary part shows complementary behavior, both tracing the hybridization dynamics anticipated by perturbation theory (c.f Section 2.2.5).

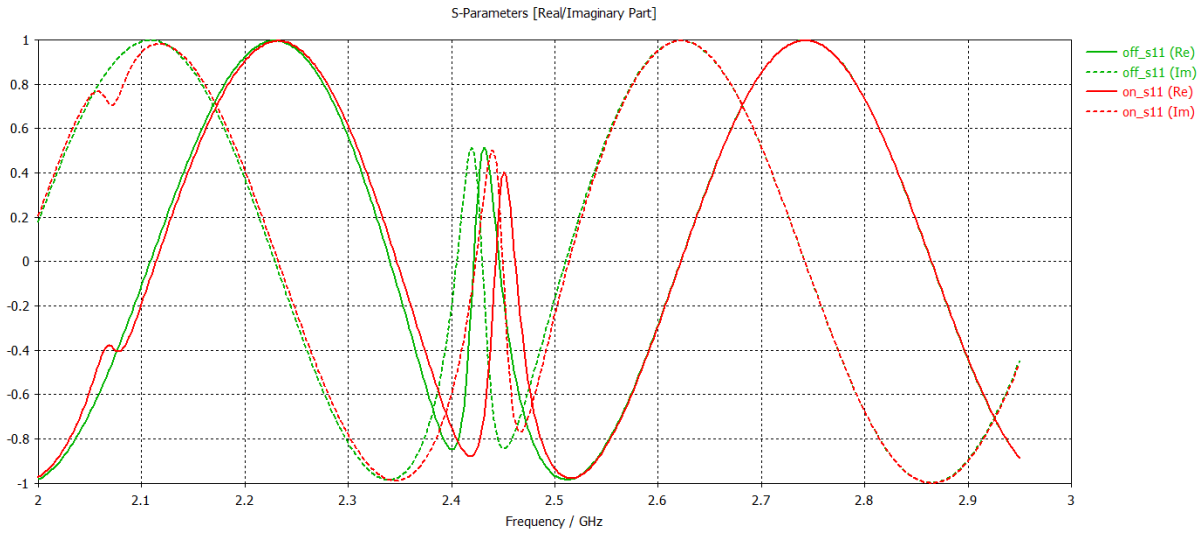

Figure 10: Real and imaginary parts of S_{11} as a function of frequency.

The splitting of resonant features between the two states illustrates the system's ability to toggle between different coupling regimes, thus modulating the phase and magnitude responses. This detailed behavior reflects the theoretical derivations where geometric perturbations (Eq. 13) and material variations (Eq. 16) shift the eigenfrequencies and affect the stored and dissipated energy within the structure (Eq. 4).

Parametric studies further elucidate the system's sensitivity to geometric and material variations. The variation of parameter y_2, shown on Fig. 11, shows shifts in the phase transition curves, underscoring the system's sensitivity to geometric tolerances, a phenomenon anticipated by the perturbation model of resonance frequency (Eq. 11). Similar shifts are observed when varying parameter x_6, Fig. 12. These results confirm the importance of precise fabrication tolerances, as even small geometric changes can result in substantial shifts in the resonance behavior. This is theoretically consistent with the dependence of f_0 on L and C (Eq. 11), which are geometrically determined, and with the Bethe-Bouwkamp scaling for subwavelength coupling (c.f Section 2.2.3).

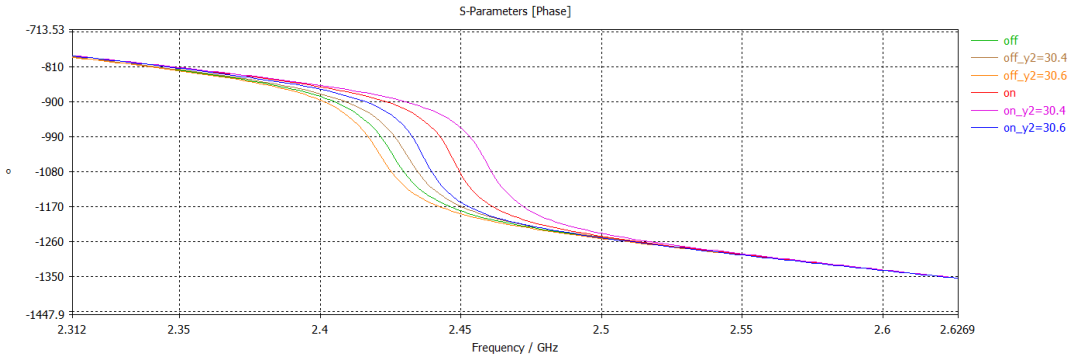

Figure 11: Phase response variation with parameter y_2.

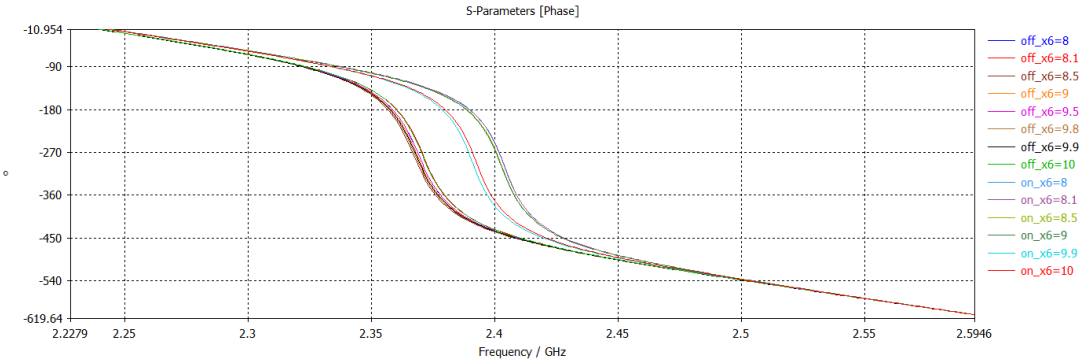

Figure 12: Phase response variation with parameter x_6.

The influence of the thickness parameter t_0, seen in Fig. 13, reveals a degree of robustness in the design with minimal impact on the phase transition characteristics. This observation suggests that the metasurface exhibits stable behavior under slight thickness variations as described in the theoretical analysis of cavity perturbations and field dynamics (c.f. Section 2.2.5).

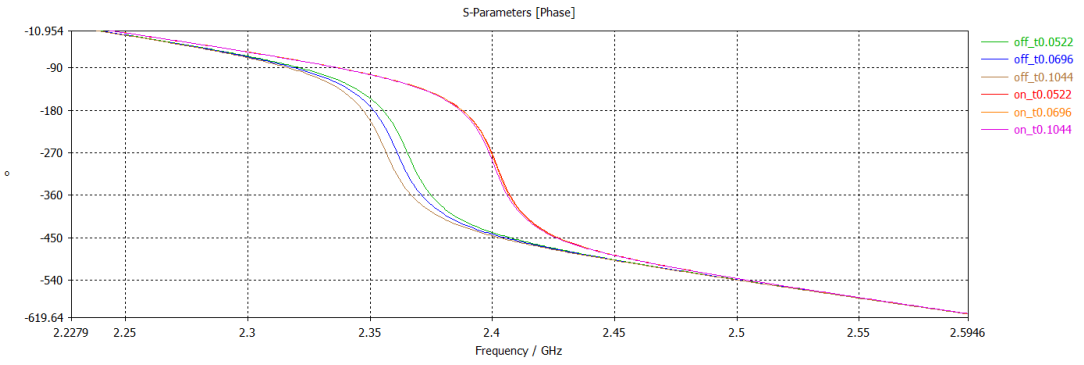

Figure 13: Phase response variation with parameter t_0.

The simulation results provide a comprehensive validation of the theoretical models presented in the preceding chapters. They demonstrate the metasurface's capacity for tunable phase and magnitude control through hybridized resonance mechanisms, with responses closely tied to geometric design, dielectric properties, and coupling dynamics. The insights gained from these simulations not only confirm the feasibility of the design but also offer guidelines for practical implementation.

2.4 Experimental Setup and Results

The final geometric layout of the tunable metasurface unit cell is shown in Fig. 14.

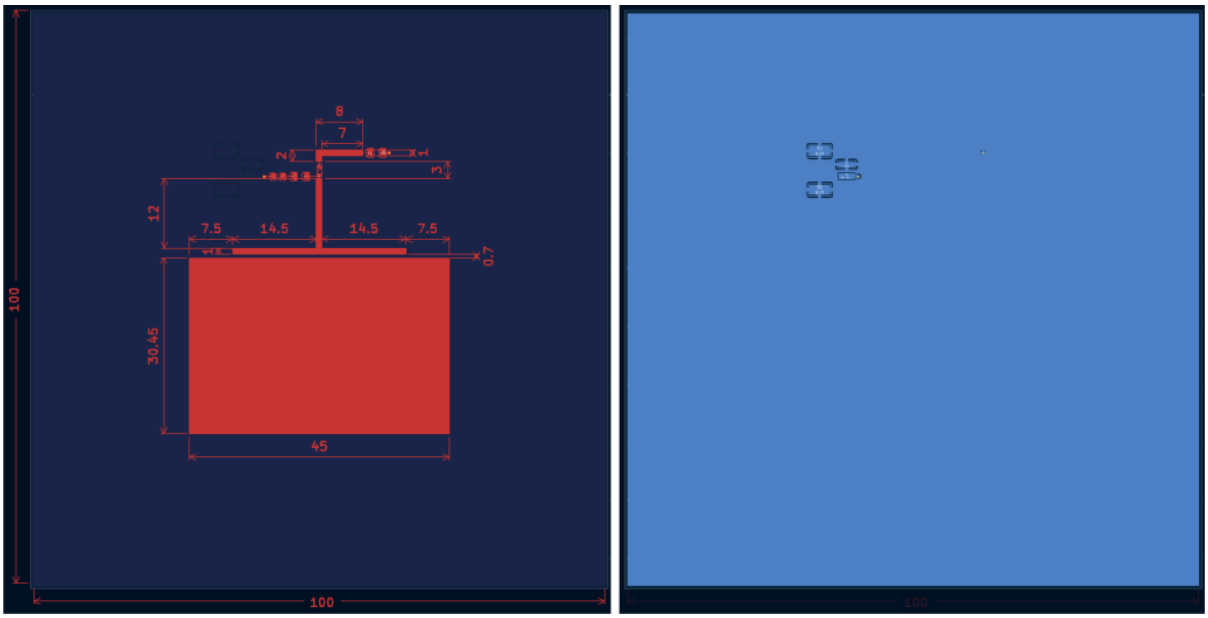

Figure 14: Layout of the metasurface unit cell, all dimensions in millimeters.

Each unit cell incorporates a DC biasing network, as shown in Figure 15. A 39nH inductor (L1 and L2), model LQW2BAS39NG00L, was selected for its self-resonance near 2GHz, ensuring effective isolation of the DC bias path from RF signals. A 39Ω series resistor (R1) sets the bias current. The PIN diode used is the Skyworks SMP1345-079LF (D1), chosen for its fast-switching behavior suitable for GHz-range modulation[11]. This configuration enables reliable diode switching with minimal RF reflection and supports a clean binary phase shift.

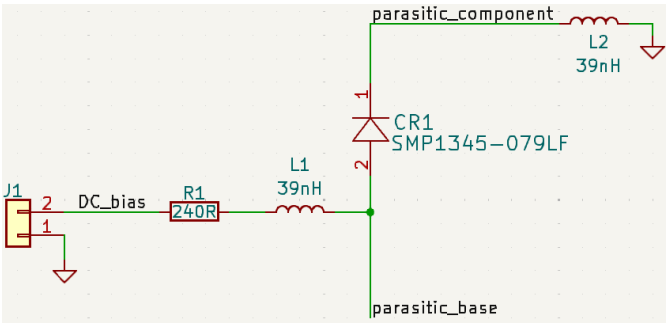

Figure 15: Schematic of the metasurface biasing circuit.

The back plane is implemented as a solid copper ground plane. To streamline manufacturing, additional spacing was added around the pins, as illustrated in Fig. 14 otherwise, soldering would have been quite complicated.

[11]Selected based on [28]

An external surface-mount connector was also included, allowing for the use of custom-crimped cables to ensure mechanical robustness. This addition facilitates reliable communication between the hardware and the Raspberry Pi 5 (RP5), which is used to control the PIN diodes via its GPIOs. The diodes were specifically chosen to have a forward current of 10mA, matching well with the RP5's typical GPIO driving current of $\sim$ 15mA.

Fig. 16 shows the fully fabricated and soldered metasurface array, consisting of 25 unit cells arranged in a 5×5 grid. The use of wider pads during the design phase, along with solder paste during assembly, helped minimize solder lines, thereby reducing parasitic capacitance that could otherwise arise from them.

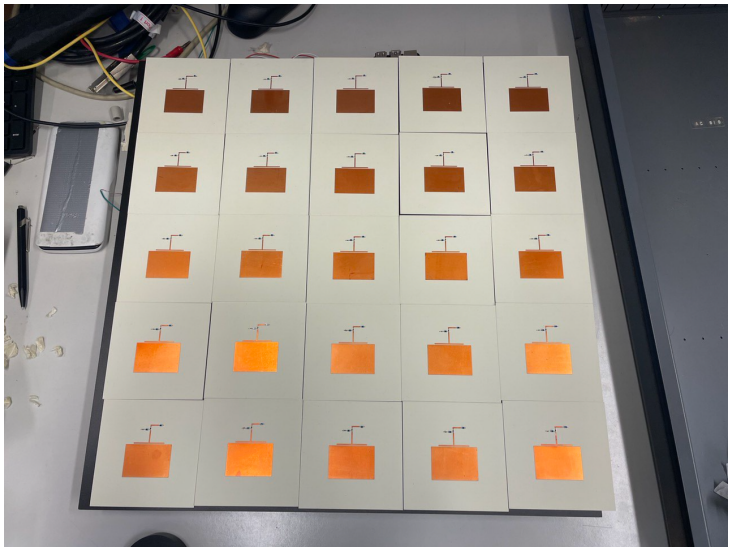

Figure 16: Assembled metasurface

Finally, the antenna phased array was mounted on a simple PVC sheet as seen in Fig. 17. Holes were drilled to accommodate the connectors, and custom 3D-printed supports were attached to slightly elevate the sheet. This provided enough clearance to route all the cables neatly underneath the structure. The Raspberry Pi 5 (RP5) was also positioned beneath the array to minimize potential electromagnetic interference and maintain a clean layout.

Figure 17: Base of metasurface

Finally, the entire assembled structure was placed inside a microwave cavity, as shown in Fig. 18. An antenna was mounted on the top surface of the cavity, and a steel cover was added to enclose the front, completing the shielding enclosure.

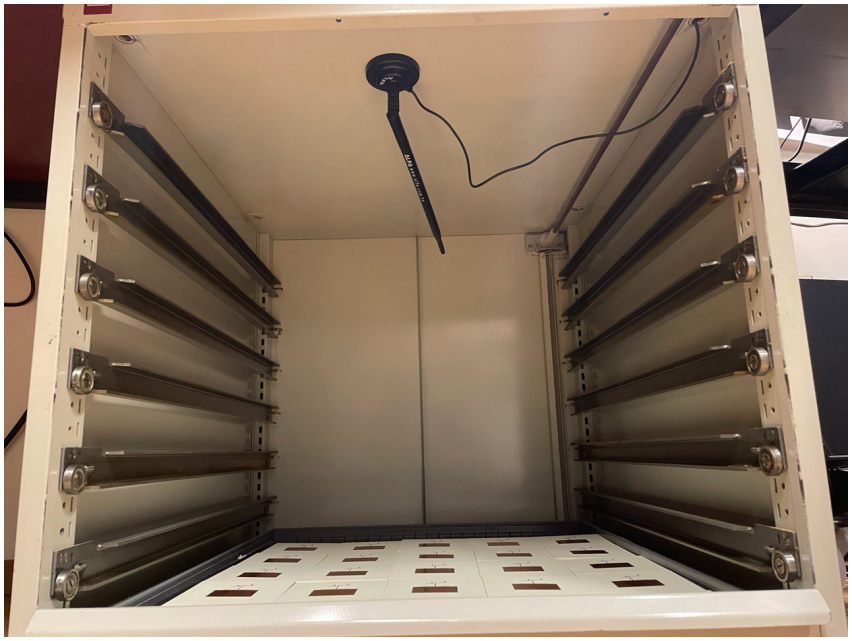

Figure 18: Completed microwave cavity with metasurface and antenna

The reflection coefficient S_{11} was measured using a Vector Network Analyzer (VNA) over the $2.4 - 2.6$GHz frequency band. The objective of this project was to characterize the metasurface as a whole; consequently, only two global states were investigated: all unit cells on or all off. Due to time constraints, partial or patterned configurations were left as future work (cf. Section 2.5).

As shown in Fig. 19, the off-state response exhibits a resonance near 2.463GHz, characterized by a dip in the S_{11} magnitude and a sharp phase of $44.66°$. This indicates strong resonant absorption and confirms that the structure supports a well-defined resonant mode when the diode is non-conducting.

In contrast, the on-state response, shown in Fig. 20, displays a shifted resonance profile. The dip in magnitude is reduced, and the phase is now at $-145.08°$. This behavior is consistent with the diode's transition to a low-impedance conducting state.

The phase shift between the on and off states at 2.4627GHz was measured to be $189.74°$. This experimentally confirms the metasurface's binary phase control capability, demonstrating its ability to toggle between two distinct electromagnetic states. Note that the operating frequency of 2.4627GHz is different from the 2.437GHz in the simulations. This can be attributed to manufacturing tolerances. This relates to Section 2.2.3, where we showed how minor changes can have significant impacts on operational frequency.

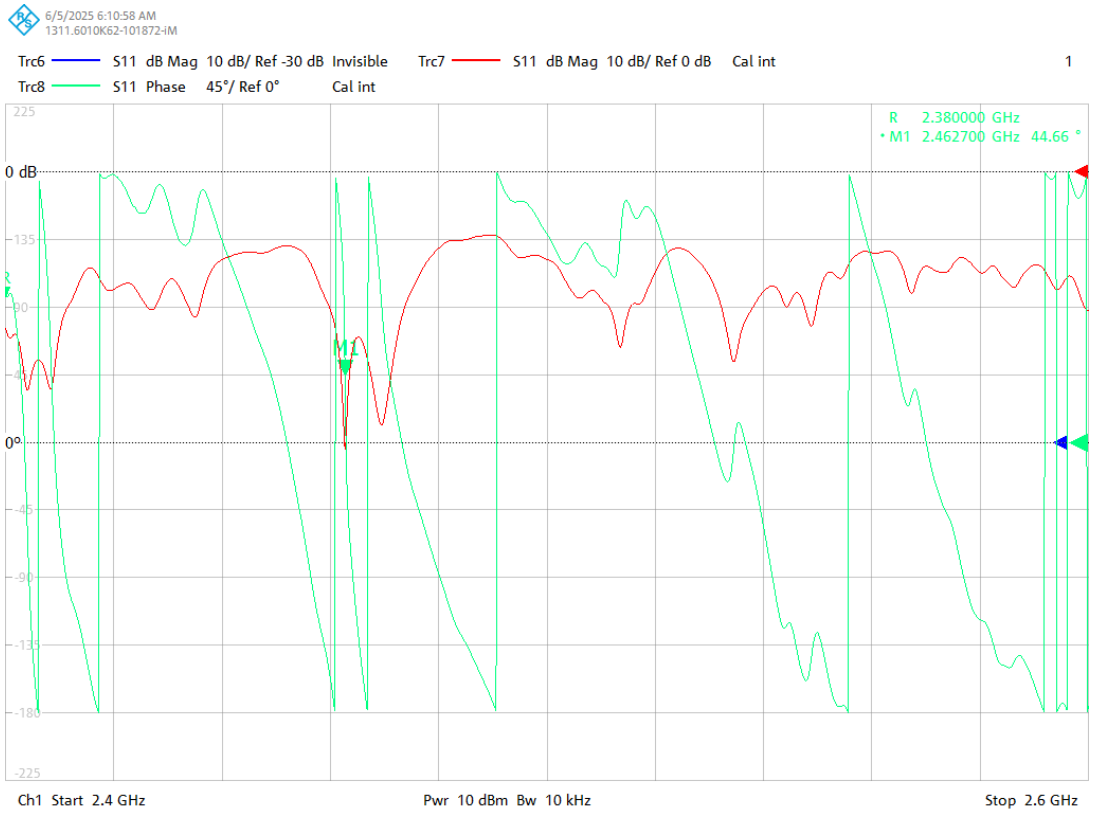

Figure 19: S_{11} magnitude and phase with diode reverse-biased (off-state).

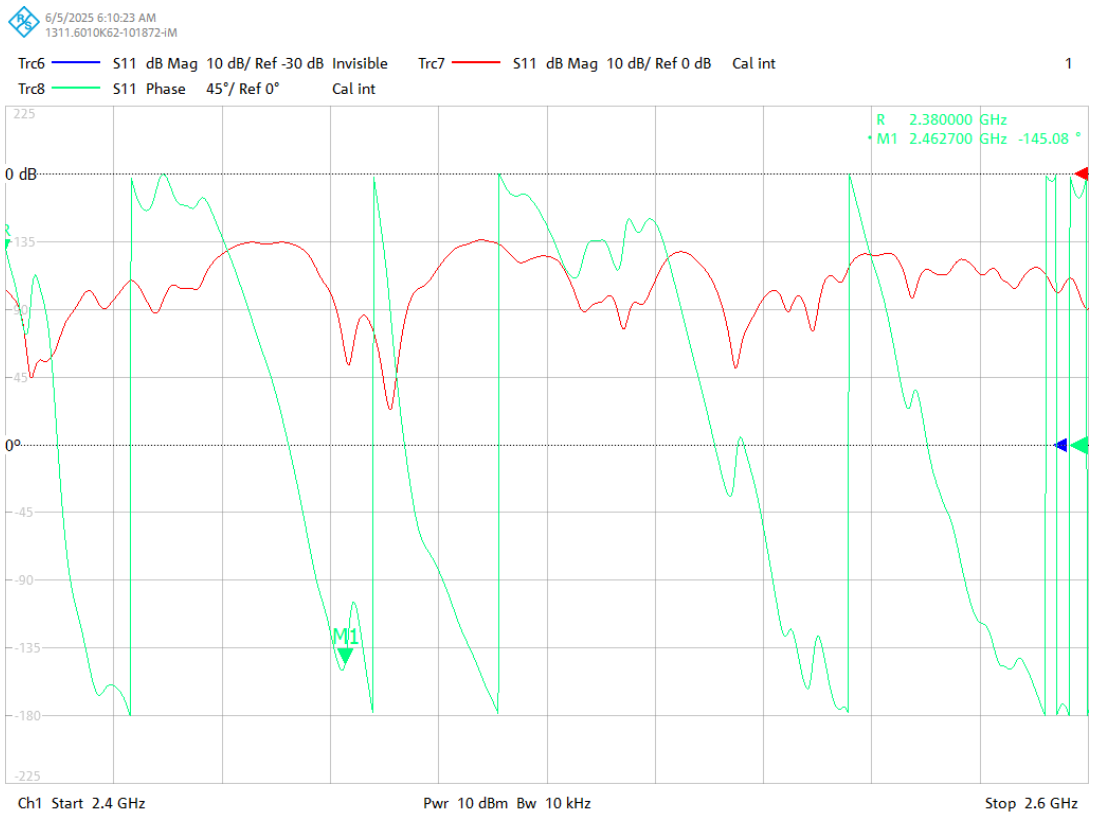

Figure 20: S_{11} magnitude and phase with the diode forward-biased (on-state)

The effects of intercell and intracell coupling can be seen in Fig. 21, 22. Within the designed bandwidth, the phase response shows clear modulation between different states, indicating strong coupling effects. Outside this band, the phase remains nearly uniform, with only minor shifts. This behavior highlights the frequency-selective nature of the coupling and echoes the mechanism discussed in Section 2.2.5, where each unit cell interacts both with the incident wave (intercell), Eq. 18, and with neighboring cells (intracell), Eq. 20.

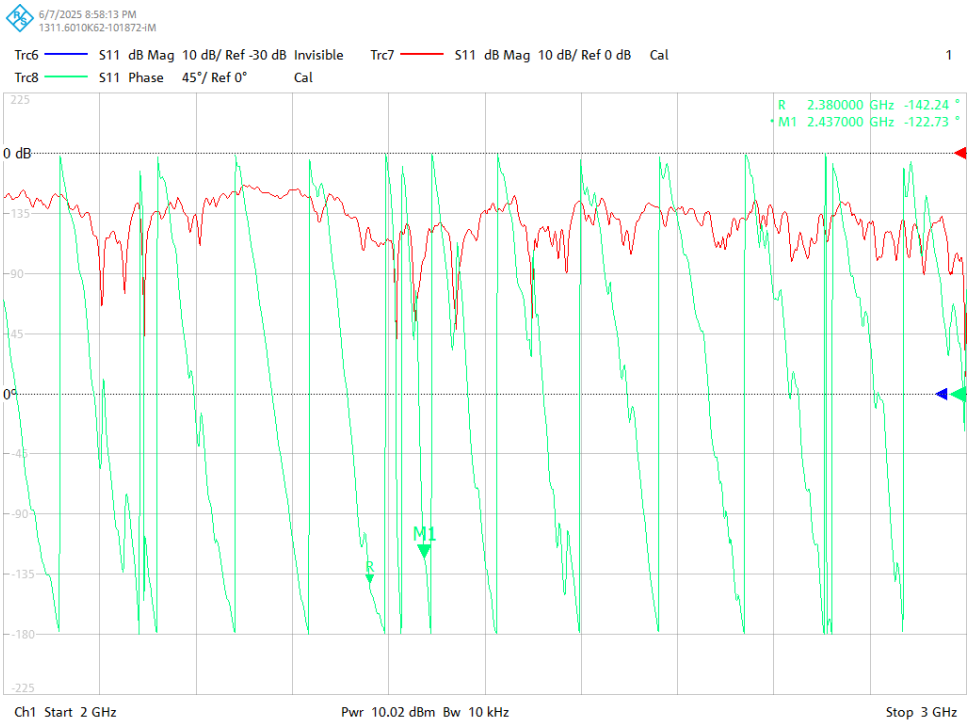

Figure 21: Whole spectrum with all unit cells on

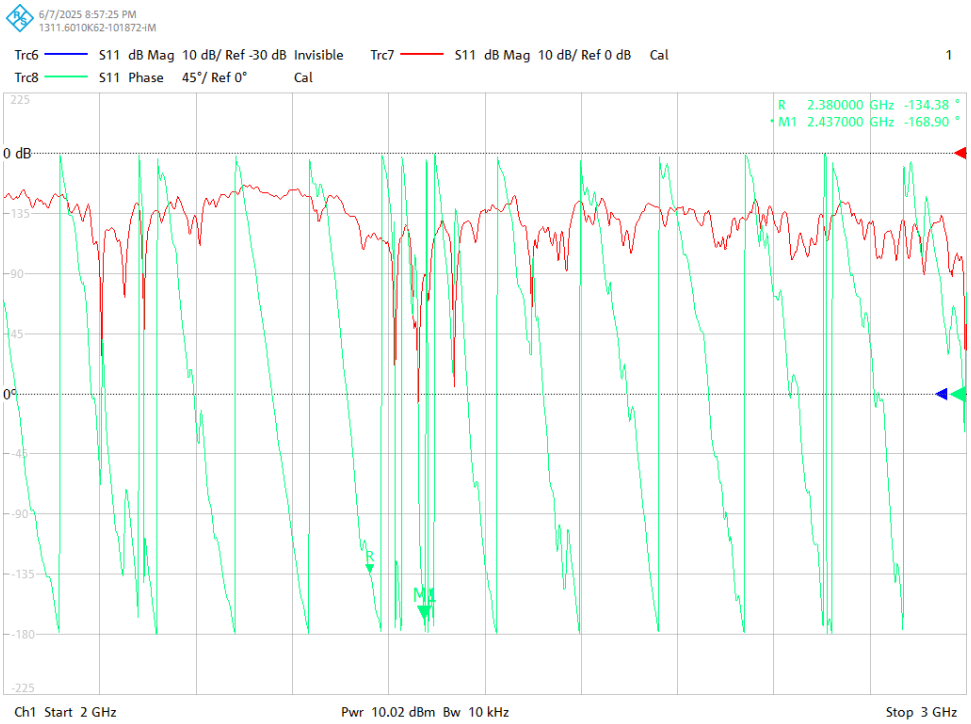

Figure 22: Whole spectrum with all unit cells off

2.5 Conclusion

This chapter established the design, simulation, and experimental validation of a binary, reconfigurable microwave metasurface capable of inducing discrete phase shifts through hybridized resonant elements controlled by PIN diodes. Theoretical analysis of dielectric loss, geometric sensitivity, and coupled mode dynamics (Section 2.2) guided the design process. Simulations confirmed the viability of the concept (Section 2.3), and measurements in a chaotic microwave cavity (Section 2.4) experimentally validated a 189.74° phase shift between the diode states, confirming controllable binary operation.

While this global on/off switching behavior validates the metasurface as a reconfigurable electromagnetic surface, the next step is to move beyond global binary control and toward spatially patterned actuation. Where the individual state of each unit cell encodes a component of a computational task. For example, applying binary patterns such as ArUco markers could serve as a testbed for programmable, spatially varying electromagnetic responses—effectively turning the metasurface into a learnable field modulator.

However, the system's extreme sensitivity to mechanical tolerances and front-plate alignment complicates inverse design and reproducibility. Even a 1 mm displacement was shown to drastically alter the measurement results. This highlights the need for coupling the hardware with robust software-driven optimization that learns which unit cells to activate in response to a global objective. The physical system could then act as a learnable, nonlinear layer whose behavior is tuned not by adjusting weights in code, but by toggling physical resonators.

3 Optical GELU

3.1 Objectives

The optical project aims to demonstrate how spatially structured, incoherent light emitted from an LED matrix can leverage the Fresnel equation and wave propagation to emulate the functional behavior of conventional nonlinear activation functions. Specifically, it targets the Gaussian Error Linear Unit (GELU).

A key objective is to create the core framework, comprising both the optical setup and the supporting software for preprocessing, control, and data interpretation.

3.2 Background

3.2.1 Non-Linear Activation Functions

The two most common non-linear activation functions are the Rectified Linear Unit (ReLU) and Gaussian Error Linear Unit (GELU).

ReLU is defined as:

$$\mathrm{ReLU}(x) = \max(0, x) \tag{33}$$

The GELU function, as used in PyTorch, is approximated as:

$$\mathrm{GELU}(x) = 0.5x \left(1 + \tanh\left[\sqrt{\frac{2}{\pi}}\left(x + 0.044715x^3\right)\right]\right) \tag{34}$$

Exploring the difference between these activation functions from a Neural Network perspective is outside the scope of this project. Instead we strive to compare them from a 'physical' perspective to the Fresnel transmission coefficient for p-polarized light[12].

If we compare these three functions side by side to illustrate the motivation for our project, we obtain:

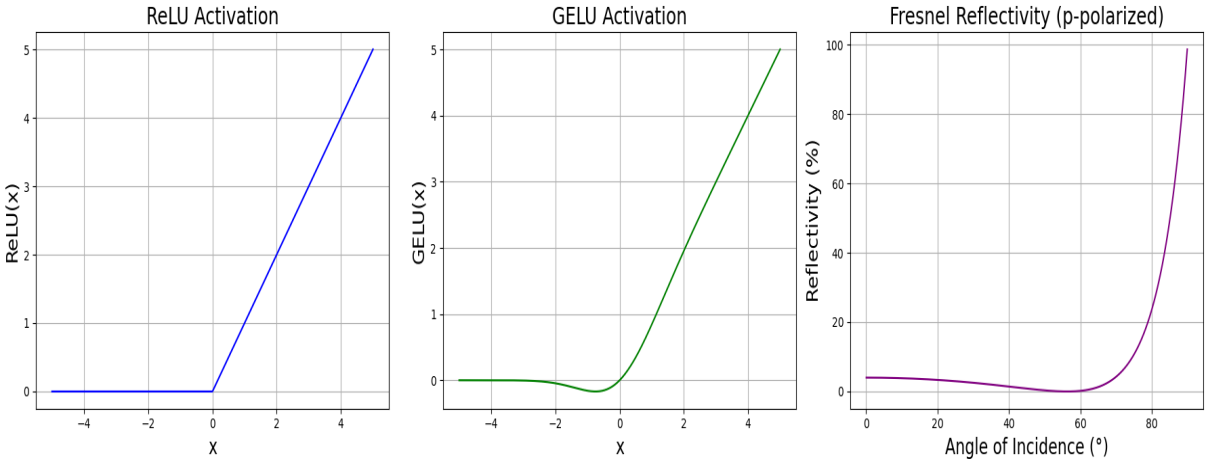

Figure 23: Graphical comparison of ReLU, GELU and Fresnel Equation

[12]Explained in detail in Section 3.2.2

Hence, the motivation for this experiment becomes quite clear. From Fig. 23, we observe a stark difference between ReLU and GELU. The former exhibits a sharp, piecewise-linear behavior, while the latter introduces a smooth, probabilistic activation curve. However, the distinction between GELU and the Fresnel reflection coefficient for p-polarized light is more subtle. Both share a smooth, sigmoidal-like shape and a continuous response. This visual resemblance hints at a shared underlying structure or principle, which our work aims to better understand and formalize.

3.2.2 Fresnel Equations

The Fresnel equations describe how an electromagnetic wave interacts with a dielectric interface. Specifically, how it splits into reflected and transmitted components when transitioning between two media with different refractive indices, n_1 and n_2. This boundary interaction is central to the project, as it enables passive control over both the amplitude and phase of the transmitted wave.

We specifically employ p-polarized light, where the electric field lies in the plane of incidence. This polarization exhibits a key property, at the Brewster angle the reflection coefficient $r_p = 0$. This results in total energy transmission into the second medium with no reflection loss. In contrast, s-polarized light (with the electric field perpendicular to the plane of incidence) does not exhibit this zero-reflection condition at any angle, making it less desirable for this application.

The amplitude transmission and reflection coefficients for p-polarized light are given by:

$$t_p = \frac{2n_1 \cos\theta_i}{n_1 \cos\theta_t + n_2 \cos\theta_i}, \tag{35}$$

$$r_p = \frac{n_2 \cos\theta_i - n_1 \cos\theta_t}{n_2 \cos\theta_i + n_1 \cos\theta_t} \tag{36}$$

Where θ_i, θ_r and θ_t are the incident, reflected and transmitted angle respectively. We can visualize this system as:

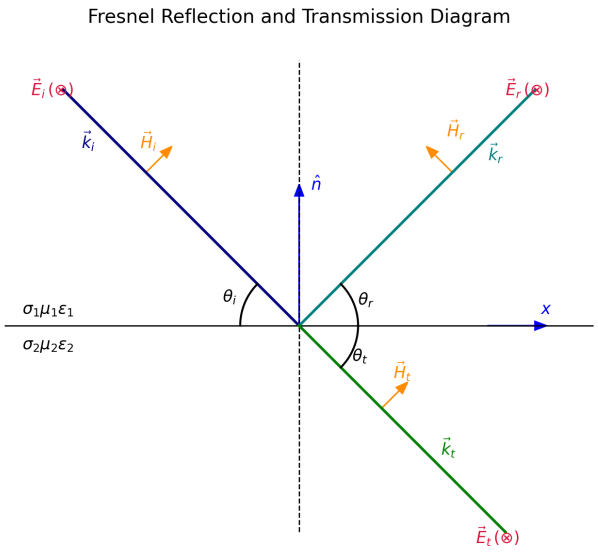

Figure 24: Physical context of Fresnel Equations

These expressions depend on both the angle of incidence θ_i and the transmitted angle θ_t, which are related via Snell's Law:

$$n_1 \sin\theta_i = n_2 \sin\theta_t \tag{37}$$

To evaluate how much power is reflected or transmitted at the interface, we define the corresponding intensity coefficients:

$$T_p = \frac{n_2 \cos\theta_t}{n_1 \cos\theta_i} |t_p|^2, \tag{38}$$

$$R_p = |r_p|^2 \tag{39}$$

These quantify the fractional power transmitted and reflected, respectively. At the Brewster angle:

$$\theta_B = \arctan\left(\frac{n_2}{n_1}\right) \tag{40}$$

we obtain $R_p = 0$, and $T_p \to 1$, maximizing transmission while preserving phase continuity. This enhances the quality and efficiency of the system by minimizing undesired reflections and maximizing deterministic field modulation.

3.2.3 Wave propagation

The planar LED matrix functions as a reconfigurable, discretized light source, where each pixel corresponds to an input vector $\mathbf{x}$. Inputs are mapped to lateral displacements d from the optical axis, which define emission angles θ as:

$$\theta = \arctan\left(\frac{d}{f}\right) \approx \frac{d}{f} \tag{41}$$

where the paraxial approximation $\theta \ll 1$ holds for small angles. f is the focal length of the lens after the screen.

Each LED emits incoherent light, producing an electric field $E_i(\mathbf{r}, t)$ with a rapidly fluctuating phase. Because the LEDs are mutually incoherent, the total intensity observed at a point $\mathbf{r}$ is the sum of the individual intensities:

$$I_{\text{total}}(\mathbf{r}) = \sum_{i=1}^{N} |E_i(\mathbf{r})|^2 \tag{42}$$

There are no cross-terms, $E_i E_j^* = 0$ for $i \neq j$, since the fields are statistically uncorrelated. This results in a smooth, speckle-free intensity profile that is robust to environmental noise and phase instabilities. This incoherent summation enables each pixel to act as an independent input channel.

Moreover, the emission profile of planar LEDs follows Lambert's cosine law, meaning their radiant intensity varies according to:

$$I(\theta) = I_0 \cos\theta \tag{43}$$

where I_0 is the peak intensity along the surface normal. This angular dependence arises from geometry. Although light is emitted isotropically within the LED's semiconductor material, the apparent emitting area decreases by $\cos\theta$ for an observer or lens at angle θ.

This relationship can be derived by considering a differential surface patch dA emitting into a solid angle $d\Omega$. The flux received by a detector at angle θ is proportional to the projected area $dA\cos\theta$ (by trigonometry), giving:

$$d\Phi \propto dA\cos\theta\, d\Omega \quad \Rightarrow \quad I(\theta) = \frac{d\Phi}{d\Omega} \propto \cos\theta \tag{44}$$

This cosine falloff does not imply that the LED emits less power at wider angles, only that the same power is geometrically redistributed over a larger apparent surface. A graphical intuition for this can be seen in Figure 25:

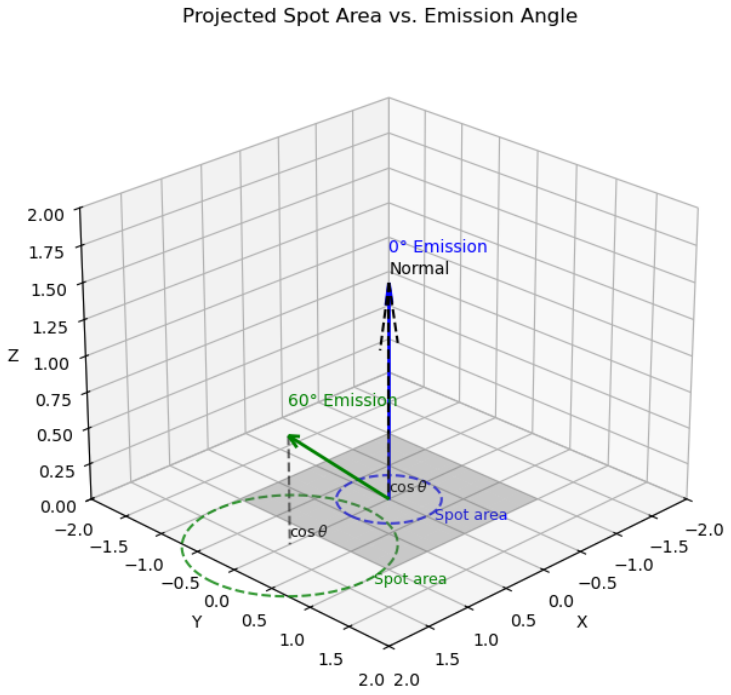

Figure 25: Graphical intuition for projected area dependence of angle

This figure illustrates how, for an emission angle of $\theta = 60°$, the projected spot area on the surface is twice as large as for normal incidence ($\theta = 0°$). Since $I(\theta) \propto \cos\theta$, and $\cos 60° = 0.5$, the same emitted power is distributed over an area that is $1/\cos\theta = 2$ times larger. This geometric scaling is the core of Lambert's cosine law.

This has two important implications for the optical setup. First, off-axis emitters contribute less light to the final intensity pattern due to the cosine angular falloff, naturally introducing a spatial weighting. Second, the optical response is inherently non-uniform as each pixel's contribution depends on its emission angle and the corresponding projected intensity. When combined with the angle-dependent modulation introduced by the interface, this behavior should enable the system to achieve our objective.

3.3 Experimental Setup and Results

The optical system was designed to project and manipulate structured light fields emitted from a programmable 64×64 LED array. Fig. 26 shows the physical cavity and layout. A linear polarizer at the input of the system ensures the selection of p-polarized light.

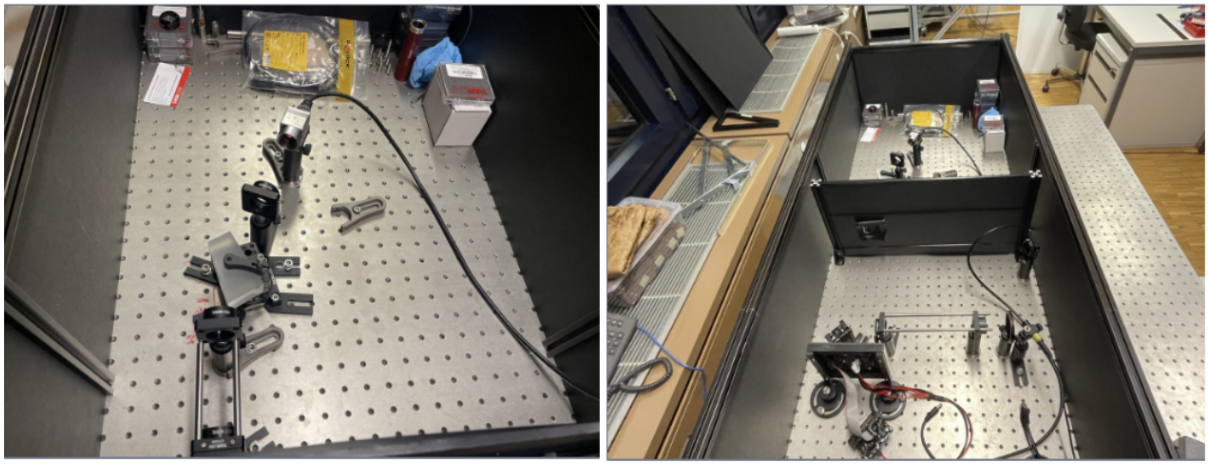

Figure 26: Photograph of the experimental optical cavity. Left: close-up of the alignment stage and lens mounts. Right: full optical path.

During testing, it was observed that reflections of the screen off the metallic optical table generated parasitic rays, which degraded image quality. To mitigate this, a physical barrier was constructed to block unwanted reflections and improve optical performance (visible as the black cardboard wall in Fig. 26).

A functional diagram of this system can be seen in Fig. 27:

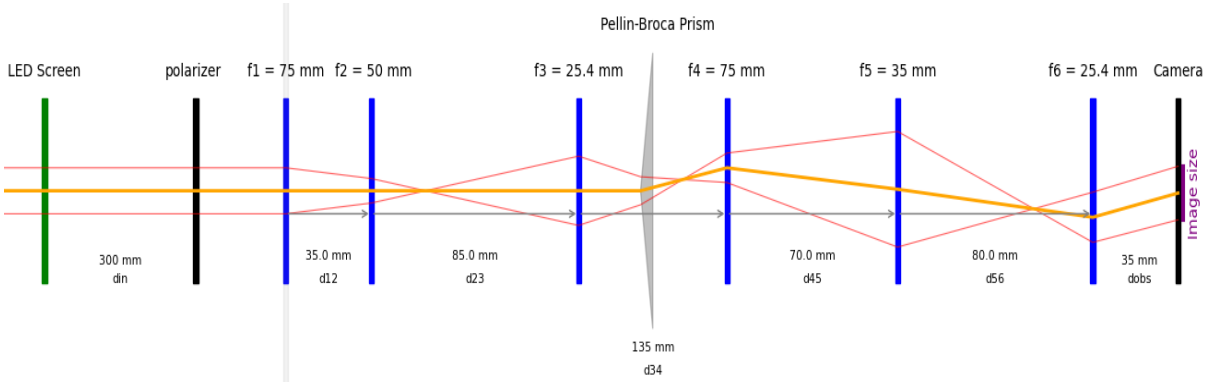

Figure 27: Schematic of the optical system. The gray vertical bar represents a physical wall in the setup. Ray paths are shown for illustrative purposes. This diagram is not to scale and is intended only for conceptual reference.

To understand how the screen is demagnified at the output, we analyze the first stage of the system, a three-lens relay composed of f_1, f_2, and f_3, as shown in Fig. 27. The LED screen is placed 300mm before lens f_1, so the object distance is:

$$s_1 = 300\text{mm} \tag{45}$$

Using the Thin lens equation:

$$\frac{1}{s_1'} = \frac{1}{f_1} + \frac{1}{s_1} = \frac{1}{75} + \frac{1}{300} = \frac{1}{60} \implies s_1' = 60\text{mm} \tag{46}$$

The second lens is placed 35mm beyond the first, so the object distance for lens f_2 is:

$$s_2 = s_1' - 35 = 25\text{mm} \tag{47}$$

This means the intermediate image is a virtual object for lens f_2, and we compute:

$$\frac{1}{s_2'} = \frac{1}{f_2} + \frac{1}{s_2} = \frac{1}{50} + \frac{1}{25} = \frac{3}{50} \implies s_2' \approx 16.7\text{mm} \tag{48}$$

The third lens is placed 85mm beyond f_2, so the object distance for f_3 is[13]:

$$s_3 = 85 - s_2' = 68.3\text{mm} \tag{49}$$

Applying the lens equation once more:

$$\frac{1}{s_3'} = \frac{1}{25.4} + \frac{1}{68.3} \Rightarrow s_3' \approx 18.5\text{mm} \tag{50}$$

The overall magnification is the product of the transverse magnifications of the three lenses:

$$M = \left(\frac{s_1'}{s_1}\right)\left(\frac{s_2'}{s_2}\right)\left(\frac{s_3'}{s_3}\right) = \left(\frac{60}{300}\right)\left(\frac{16.7}{25}\right)\left(\frac{18.5}{68.3}\right) \approx 0.036 \tag{51}$$

Thus, the system produces a straight, highly demagnified image of the LED pattern. The resulting image quality is sharp and aberration-minimized, as demonstrated in the projected calibration pattern shown in Fig. 28.

[13]This follows from the convention that object distance s is measured from the lens to the object, positive if the object is to the left of the lens (i.e., a real object). Since the image formed by f_2 lies 16.67mm before f_3, and the separation between f_2 and f_3 is 85mm, the object distance for f_3 is computed as $s_3 = 85 - 16.67$

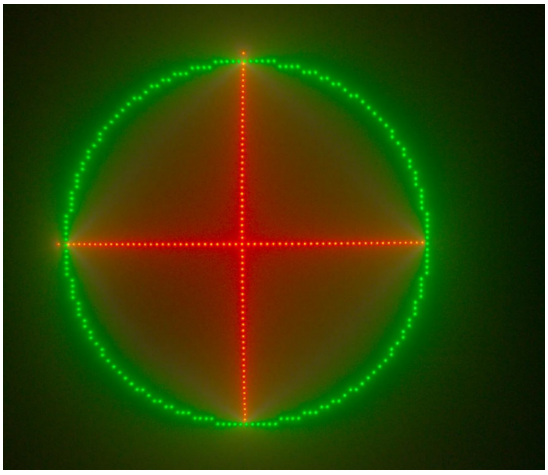

(a) Image as seen from camera

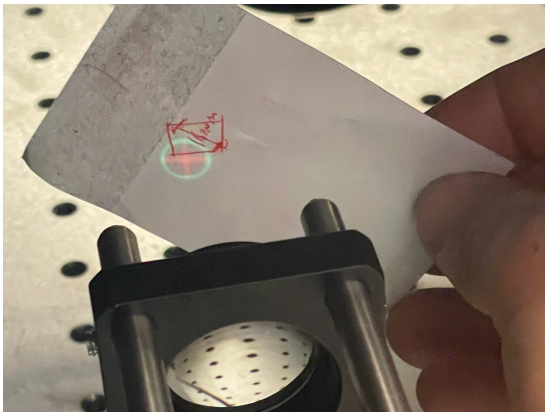

(b) Image as seen by observer

Figure 28: Calibration pattern from the LED array projected through the full optical setup. Confirms image quality, proper focus, and alignment.

To evaluate whether the emission from all LEDs would collectively form a coherent field envelope, we activated every pixel and recorded the spatial intensity. Since the LEDs are mutually incoherent, we expected spatial averaging to yield a uniform field. The 3D intensity surface in Fig. 29 confirms this: the resulting field is effectively planar, with only minor pixel-to-pixel intensity fluctuations.

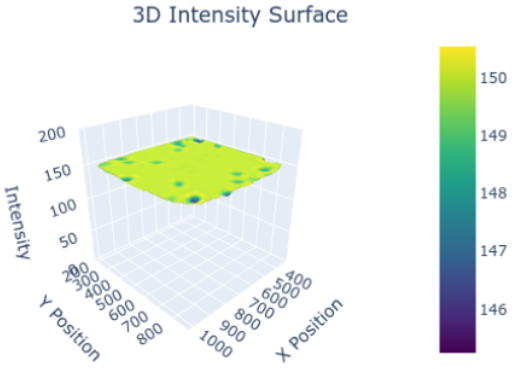

Figure 29: 3D intensity distribution with all LEDs turned on. The resulting planar wavefront confirms incoherent field averaging and system uniformity.

To validate phase propagation and spatial resolution in the system, a coherent, polarized laser beam was injected into the same optical path. The resulting intensity pattern at the output plane, Fig. 30, exhibits a fringe-like structure and central symmetry, consistent with a Fresnel diffraction envelope. While not an ideal or interpretable response, the structured pattern confirms that the system supports phase-coherent transport and that no major aberrations or misalignment dominate the beam path. This visual check provides a reference for interpreting results under incoherent illumination.

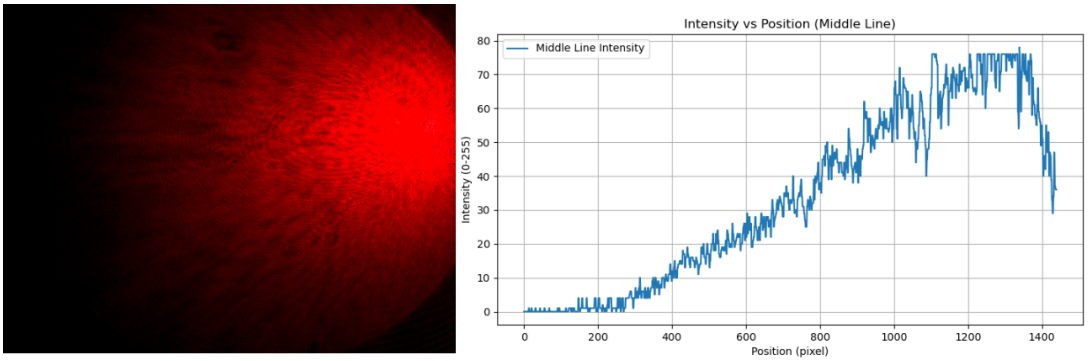

Figure 30: Coherent laser injected through the system produces a Fresnel-like interference pattern. Confirms phase-preserving optical path and proper imaging alignment.

Now we test the whole pipeline as shown in Fig. 31. The system's output reveals a structured yet irregular intensity profile. While this confirms that the optical system responds nonlinearly to changes in input angle, the observed behavior lacks the smooth, asymmetric, and saturating characteristics of a GELU-like transformation. Instead, the pattern suggests strong angular sensitivity with unintended divergence or distortion, making it unsuitable in its current form.

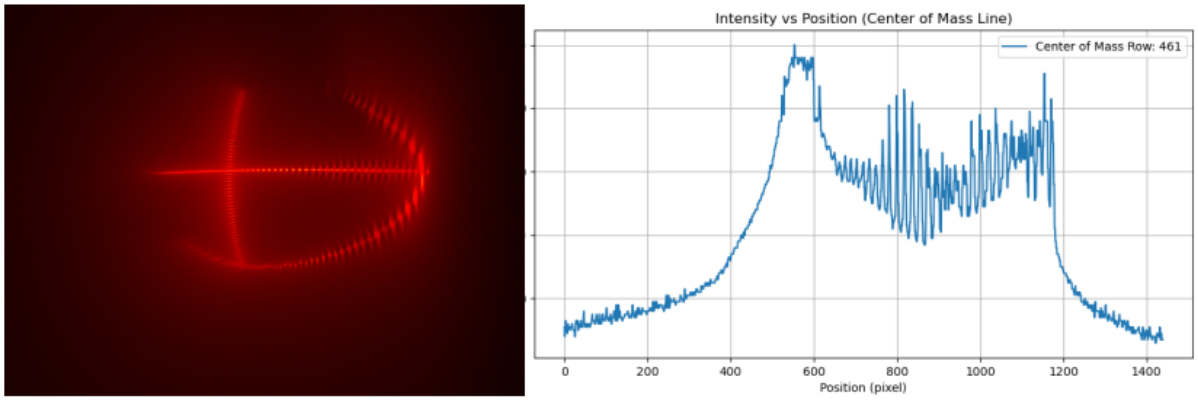

Figure 31: Interference pattern observed under selective pixel activation. The irregularity confirms high spatial sensitivity and supports programmable field shaping.

This result highlights a mismatch between the intended nonlinear mapping and the system's actual response. The complexity and asymmetry of the output indicate that even small angular variations at the input result in amplified and spatially inconsistent intensity shifts at the output plane. To understand the root of this mismatch, we next examine the system's optical structure by using its transfer matrix.

We model the extended six-lens system using ABCD ray-transfer matrices. The full system includes six lenses (f_1 through f_6) and seven propagation distances ($d_{in}, \ldots, d_{obs}$), with a Pellen–Broca prism inserted between f_3 and f_4. The total system matrix is given by:

$$\begin{aligned} M = T(d_{obs}) \cdot L(f_6) \cdot T(d_{56}) \cdot L(f_5) \cdot T(d_{45}) \cdot L(f_4) \cdot T(d_{34}) \cdot P \cdot \\ L(f_3) \cdot T(d_{23}) \cdot L(f_2) \cdot T(d_{12}) \cdot L(f_1) \cdot T(d_{in}) \end{aligned} \tag{52}$$

where each element is defined by:

$$L(f) = \begin{bmatrix} 1 & 0 \\ -1/f & 1 \end{bmatrix} \tag{53}$$

$$T(d) = \begin{bmatrix} 1 & d \\ 0 & 1 \end{bmatrix} \tag{54}$$

$$P = \begin{bmatrix} 1 & 0 \\ 0 & 1 \end{bmatrix} \tag{55}$$

The polarizer is excluded from this analysis, as it modifies only the polarization state, not the geometric propagation. The Pellen–Broca prism introduces angular deviation and beam displacement, but is approximately treated as an identity transform in ABCD analysis when ray angles remain small and collimation is preserved. More accurate modeling would involve an angular beam steering matrix or coordinate transformation.

Substituting the numerical values, we obtain the overall ABCD matrix:

$$\begin{aligned} M = & \begin{bmatrix} 1 & 35 \\ 0 & 1 \end{bmatrix} \cdot \begin{bmatrix} 1 & 0 \\ -\frac{1}{25.4} & 1 \end{bmatrix} \cdot \begin{bmatrix} 1 & 80 \\ 0 & 1 \end{bmatrix} \cdot \begin{bmatrix} 1 & 0 \\ -\frac{1}{35} & 1 \end{bmatrix} \cdot \begin{bmatrix} 1 & 70 \\ 0 & 1 \end{bmatrix} \cdot \begin{bmatrix} 1 & 0 \\ -\frac{1}{75} & 1 \end{bmatrix} \cdot \\ & \begin{bmatrix} 1 & 135 \\ 0 & 1 \end{bmatrix} \cdot \begin{bmatrix} 1 & 0 \\ -\frac{1}{25.4} & 1 \end{bmatrix} \cdot \begin{bmatrix} 1 & 85 \\ 0 & 1 \end{bmatrix} \cdot \begin{bmatrix} 1 & 0 \\ -\frac{1}{50} & 1 \end{bmatrix} \cdot \begin{bmatrix} 1 & 35 \\ 0 & 1 \end{bmatrix} \cdot \begin{bmatrix} 1 & 0 \\ -\frac{1}{75} & 1 \end{bmatrix} \cdot \begin{bmatrix} 1 & 300 \\ 0 & 1 \end{bmatrix} \end{aligned} \tag{56}$$

Therefore:

$$M = \begin{bmatrix} 1.42 & -339.90 \\ 0.08 & 17.67 \end{bmatrix} = \begin{bmatrix} A & B \\ C & D \end{bmatrix} \tag{57}$$

The nonzero element $C = 0.08\,\mathrm{mm}^{-1}$ indicates that the system has net positive optical power, corresponding to an effective focal length of

$$f_{\text{eff}} = \frac{1}{C} = \frac{1}{0.08\,\mathrm{mm}^{-1}} = 12.5\,\mathrm{mm}, \tag{58}$$

meaning the system is converging rather than afocal. This contributes to beam compression and intensity localization in certain regions of the output plane.

The angular magnification term $D = 17.67$ plays a critical role in shaping the system's sensitivity to input direction. For a ray entering at angle θ_{in}, the output angle is given by the ray transfer equation

$$\theta_{\text{out}} = C y_{\text{in}} + D\theta_{\text{in}}.$$

Assuming the LED matrix subtends a modest angular range of $\theta_{\text{in}} \in [-5^\circ, 5^\circ]$, or approximately ± 0.087 radians, the output angular spread becomes

$$\theta_{\text{out}} \in D \cdot \theta_{\text{in}} \approx 17.67 \cdot [-0.087, 0.087] \approx [-1.54, 1.54] \text{ radians} \approx [-88^\circ, 88^\circ].$$

This nearly full-hemisphere spread indicates an extreme amplification of small angular differences, leading to high sensitivity and instability in the spatial intensity profile at the output.

The matrix element $A = 1.42$ implies moderate lateral magnification:

$$y_{\text{out}} = A y_{\text{in}} + B\theta_{\text{in}},$$

which suggests that displacements in the input plane are also expanded by a factor of 1.42 at the output. However, the dominating contribution comes from the B term, with $B = -339.90\,\text{mm}$, which introduces a large angular-to-spatial coupling. Specifically, rays entering with nonzero angle θ_{in} are displaced at the output by

$$y_{\text{out}} \supset B\theta_{\text{in}} \approx -339.90\,\text{mm} \cdot \theta_{\text{in}}.$$

Even for small angles, say $\theta_{\text{in}} = 0.05$ radians ($\approx 2.86^\circ$), this results in a displacement of

$$y_{\text{out}} \approx -339.90\,\text{mm} \cdot 0.05 \approx -17\,\text{mm},$$

which is substantial. This confirms that the system produces virtual images far outside the physical bounds of the optical assembly, leading to rapid beam divergence and the irregular output distributions seen in Fig. 31.

Overall, the ABCD matrix shows that the system behaves as a converging, angularly magnifying, and spatially dispersive relay. These properties explain the failure to reproduce a smooth, monotonic, GELU-like transformation. Instead of compressing angular inputs into a predictable sigmoid-like intensity profile, the system spreads and distorts them, creating highly structured and unpredictable outputs. This mismatch motivates a redesign of the optical layout to suppress angular magnification (D), reduce beam divergence (smaller $|B|$).

3.4 Processing Algorithms

Raw images captured by the camera include significant noise, ambient light, and optical distortion. To extract meaningful we apply a multi-stage processing pipeline.

The process begins with the raw optical input, as shown in Fig. 32. Each spot corresponds to a light source from the LED matrix that has propagated through the cavity and optical system.

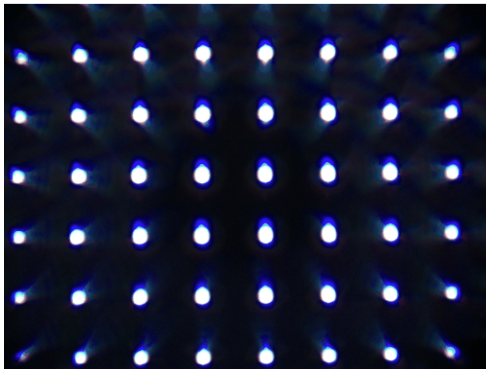

Figure 32: Raw optical image captured from the LED matrix after propagation through the optical system.

To isolate the actual diffraction spots from background illumination, we apply binary thresholding:

$$T(x) = \begin{cases} 1, & \text{if } I(x) \geq \tau \\ 0, & \text{otherwise} \end{cases}, \tag{59}$$

where $I(x)$ is pixel intensity and τ is empirically chosen. Fig. 33 shows the result: a clean binarized image that highlights high-intensity optical features.

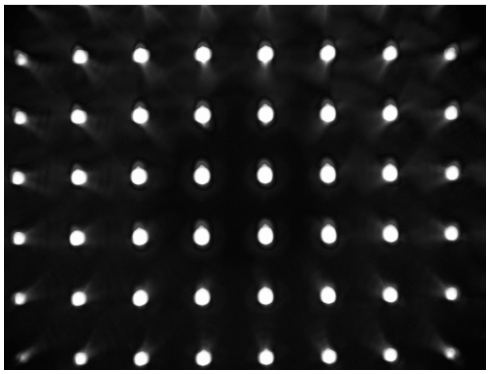

Figure 33: Binarized image after thresholding, showing optical hotspots corresponding to active LED elements.

Next, we apply morphological filtering to suppress noise and smooth the detected shapes. This includes erosion, dilation, opening, and closing using cross-shaped structuring elements:

$$(I \oplus S)(x) = \max_{s \in S} I(x - s), \tag{60}$$

$$(I \ominus S)(x) = \min_{s \in S} I(x + s). \tag{61}$$

These operations remove isolated noise pixels and sharpen blob boundaries. Fig. 34 shows the effect of morphology, yielding clean and connected components.

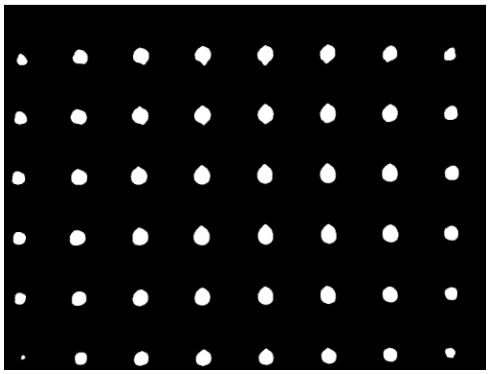

Figure 34: Post-morphological filtering. Unwanted noise is removed and features are consolidated.

From the cleaned binary image, we extract contours and compute shape statistics. Each diffraction spot is modeled as an ellipse using moments:

$$M_{pq} = \sum_{x,y} x^p y^q I(x, y), \tag{62}$$

with centroids:

$$c_x = \frac{M_{10}}{M_{00}}, \quad c_y = \frac{M_{01}}{M_{00}}. \tag{63}$$

These are then fitted to ellipses by minimizing the conic section error:

$$Ax^2 + Bxy + Cy^2 + Dx + Ey + F = 0. \tag{64}$$

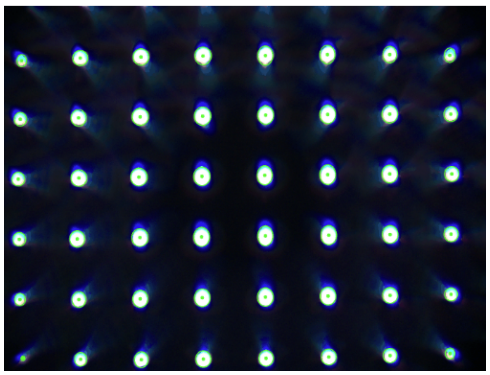

Figure 35: Elliptical fits superimposed on the extracted features

For each detected feature (ellipse), we define a region mask $M_e(x)$ and compute the mean optical intensity:

$$I_e = \frac{\sum_{x \in M_e} I(x)}{|M_e|}, \tag{65}$$

which estimates the total optical power delivered to that spatial region.

3.5 Conclusion

This chapter explored the use of structured incoherent light, modulated by a programmable LED matrix and passed through a multilens optical system, to approximate nonlinear activation functions such as GELU. Beginning with theoretical motivation rooted in the similarity between the Fresnel transmission curve and GELU (Section 3.2), the optical setup (Section 3.3) was designed to map input angles, determined by pixel position, onto output intensities. Image processing tools (Section 3.4) allowed for detailed extraction of the spatial patterns generated by selective input activation.

The system demonstrated a nonlinear transformation between angular inputs and output intensity, but not one that resembles GELU. Instead, the intensity profiles were highly irregular and angularly distorted. ABCD matrix analysis revealed a potential reason: the system amplifies input angles rather than compressing them. With $D = 17.67$ and $B = -339.90\,\text{mm}$, even modest input angles produce broad, virtual output divergence incompatible with activation-like behavior.

However, these findings also provide a roadmap for improvement. A redesigned optical system should aim to reduce angular magnification, suppress angular-to-spatial displacement. In this regime, angular variations in input could be directly mapped to output intensity in a smoother, more controlled manner—potentially achieving a GELU-like shape.

As an immediate extension, the system could be miniaturized and tested with a smaller LED array. This would assess whether the lens relay and angular mapping remain functional under constrained spatial conditions. More broadly, combining the optical system with a differentiable simulation pipeline would enable data-driven design of optical activation layers, where parameters are optimized end-to-end for a target nonlinear function.

In summary, while the current system falls short of implementing a GELU-equivalent transform, it establishes a viable experimental framework. With further refinement and task-driven design, this approach holds promise.

4 Annex

Schottky diode vs PIN Diode

In the context of high-frequency RF circuit design, particularly for metasurfaces intended for low-power nonlinear activation functions, the selection of appropriate diode components is critical. PIN diodes are uniquely suited for such applications due to their distinct physical structure and operational characteristics, which confer advantages over alternatives such as Schottky diodes. This annex has for objective to give a brief overview of the underlying mechanism of RF diodes and to justify our choice of PIN diodes.

Physical Structure and RF Behavior:

A PIN diode consists of a wide, undoped intrinsic (I) layer between p-type and n-type regions. Under forward bias, the injection of minority carriers into the I-layer floods it with charge, resulting in a plasma of electrons and holes. This plasma reduces the resistivity of the I-layer, effectively turning the diode into a low-resistance conductor for RF currents. The resistance R_i of the I-layer under forward bias can be approximated as: $R_i = \frac{L_i}{q \cdot \mu \cdot N \cdot A}$, where L_i is the intrinsic layer thickness, q is the elementary charge, μ is the carrier mobility, N is the carrier concentration, and A is the cross-sectional area.

Under reverse bias, the intrinsic region becomes fully depleted, creating a wide depletion region that presents a high impedance to RF signals. This behavior is described by the depletion capacitance C_d: $C_d = \frac{\epsilon \cdot A}{W_d}$, where ε is the permittivity of the semiconductor material, and W_d is the width of the depletion region. The large W_d of the intrinsic region results in a low junction capacitance, reducing RF signal leakage in the off state and providing high isolation.

On the other hand, Schottky diodes operate based on majority carrier conduction characterized by fast switching times and low forward voltage drops. However, their low reverse breakdown voltages and high reverse leakage currents limit their effectiveness in high-isolation, high-power RF applications. Schottky diodes also exhibit significant parasitic capacitance: $C_j \approx \frac{\epsilon \cdot A}{W_j}$ where W_j is the narrow depletion width of the Schottky barrier, leading to greater signal leakage at high frequencies.

In contrast, PIN diodes offer higher breakdown voltages and superior isolation in the reverse-biased state. The wider depletion region achieved in the intrinsic layer of the PIN structure minimizes junction capacitance and enhances isolation. Additionally, the resistivity of the I-layer under forward bias can be precisely controlled by adjusting the forward bias current I_f: $R_i(I_f) \approx \frac{V_f}{I_f}$, where V_f is the forward voltage. This predictable, tunable resistance is essential for applications such as RF switching, attenuation, and phase shifting.

PIN diodes exhibit excellent linearity and power handling capabilities, critical for high-frequency metasurface designs. The high RF isolation achieved in the off state and the low insertion loss in the on state make them ideal for modulating RF signals in dynamic metasurface arrays. The dynamic resistance R_d and capacitance C_d of the PIN diode under RF excitation can be modeled as: $Z(w) = R_d + \frac{1}{j \cdot w \cdot C_d}$ where ω is the angular frequency of the RF signal. The ability to modulate R_d via forward bias current provides

a reliable mechanism for controlling the phase and amplitude of RF signals.

The choice of PIN diodes for this project is grounded in their superior physical and electrical characteristics, including high isolation, tunable resistance, low capacitance, and excellent linearity at RF frequencies. These properties make them ideally suited for integration into dynamic metasurface arrays designed to implement physical nonlinear activation functions in low-power, high-frequency neural network architectures. The mathematical models provided herein offer a robust foundation for predicting device behavior and optimizing system performance.

This switching behavior leverages the unique properties of PIN diodes, which function as current-controlled resistors at high frequencies. When forward-biased, carriers are injected into the diode's intrinsic region, dramatically lowering resistance and enabling efficient RF conduction. In contrast, reverse bias depletes the carriers, restoring high impedance and effectively opening the RF path. This duality allows for rapid, controlled transitions between high-reflection ($\Delta\phi = \pi$) and transparent states ($\Delta\phi = 0$) within the metasurface.

Modeling Pin Diodes:

Our chosen pin diode can be modeled as two lumped elements as seen in Fig. 36

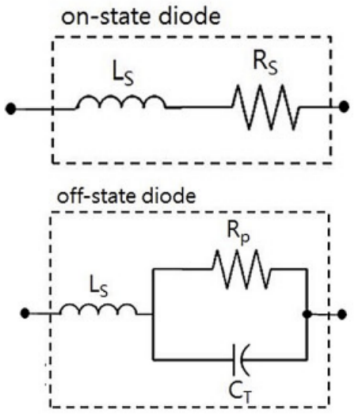

Figure 36: Modeling of PIN diode [28]

With $L_s = 0.7$nH, $R_s = 1.5\Omega$, $R_p \geq 10\text{k}\Omega$ and $C_T = 0,18$pF

5 Acknowledgments

I would like to sincerely thank my supervisor, Tim Tuuva, for his invaluable guidance, support, and patience throughout this project.

Tim's ability to calmly navigate every challenge I brought his way—whether technical or conceptual—made all the difference. His thoughtful feedback and steady encouragement kept this work on track and helped me grow through the process.

I'm especially grateful for his time, clarity, and his unwavering support during the inevitable ups and downs. This project truly would not have come together without his insight and dedication.

I would also like to thank Prof. Fleury for welcoming me into the LWE and allowing me to work on these projects over the past year.

6 Sources

[1] L. Hardesty, "Explained: Neural networks," *MIT News*, 2017. [Online]. Available: https://news.mit.edu/2017/explained-neural-networks-deep-learning-0414.

[2] P. D. Wasserman and T. Schwartz, "Neural networks. ii. what are they and why is everybody so interested in them now?" *IEEE Expert*, vol. 3, no. 1, pp. 10–15, 1988.

[3] IBM, "What is a neural network?" *IBM*, 2021. [Online]. Available: https://www.ibm.com/think/topics/neural-networks.

[4] N. Kulathunga, N. Ranasinghe, D. Vrinceanu, Z. Kinsman, L. Huang, and Y. Wang, "Effects of nonlinearity and network architecture on the performance of supervised neural networks," *Algorithms*, vol. 14, no. 2, p. 51, 2021. DOI: 10.3390/a14020051.

[5] B. Hoppenstein, "Why tech giants such as microsoft, amazon, google and meta are betting big on nuclear power," *CNBC*, 2024. [Online]. Available: https://www.cnbc.com/2024/12/28/why-microsoft-amazon-google-and-meta-are-betting-on-nuclear-power.html.

[6] A. Lawson, "Google to buy nuclear power for ai datacentres in 'world first' deal," *The Guardian*, 2024. [Online]. Available: https://www.theguardian.com/technology/2024/oct/15/google-buy-nuclear-power-ai-datacentres-kairos-power.

[7] N. Kaina, M. Dupré, G. Lerosey, and M. Fink, "Shaping complex microwave fields in reverberating media with binary tunable metasurfaces," *Scientific Reports*, vol. 4, p. 6693, 2014.

[8] N. Kaina, M. Dupré, M. Fink, and G. Lerosey, "Hybridized resonances to design tunable binary phase metasurface unit cells," *Optics Express*, vol. 22, no. 16, pp. 18 881–18 888, 2014.

[9] Olgor, *Wifi analyzer*, 2025. [Online]. Available: https://play.google.com/store/apps/details?id=abdelrahman.wifianalyzerpro.

[10] P. McNeil, "Highlights of measuring dielectrics with rf equipment part 1," *Fairwave Microwave*, 2023. [Online]. Available: https://blog.fairviewmicrowave.com/2023/01/19/highlights-of-measuring-dielectrics-with-rf-equipment-part-1/.

[11] R. Corporation, *Rogers 4000 series: High frequency circuit materials*, https://rogerscorp.com/documents/729/acm/4000-series/4000-series-brochure.pdf, 2017.

[12] I. Group, *Fr4 laminate material datasheet*, https://www.isola-group.com/wp-content/uploads/FR4-Laminate-Datasheet.pdf, 2015.

[13] D. M. Pozar, *Microwave Engineering*, 4th. John Wiley & Sons, 2011.

[14] C. M. Soukoulis, S. Linden, and M. Wegener, "Negative index metamaterials: New frontiers in optics," *Science*, vol. 315, no. 5808, pp. 47–49, 2007.

[15] H. A. Bethe, "Theory of diffraction by small holes," *Physical Review*, vol. 66, no. 7-8, p. 163, 1944.

[16] C. Bouwkamp, "Diffraction theory," *Reports on Progress in Physics*, vol. 17, no. 1, p. 35, 1954.

[17] P. L. Novotny, "Electromagnetic waveguides and resonators," 2013.

[18] H. A. Haus and W. Huang, "Coupled-mode theory," *Proceedings of the IEEE*, vol. 79, no. 10, pp. 1505–1518, 1991. DOI: 10.1109/5.104225.

[19] G. Duan, J. Schalch, X. Zhao, *et al.*, "A survey of theoretical models for terahertz electromagnetic metamaterial absorbers," *Sensors and Actuators A: Physical*, vol. 285, pp. 270–287, 2019. DOI: 10.1016/j.sna.2018.11.051.

[20] W. Huang, S.-T. Cao, W. Zhang, S. Yin, and J. Han, "Analogy to debye model in metamaterials: Resonant frequency shifting due to coupling," *Optics and Laser Technology*, 2024. [Online]. Available: https://www.sciencedirect.com/science/article/pii/S0030399223012707?ref=cra_js_challenge&fr=RR-1.

[21] K. Koshelev, S. Lepeshov, M. Liu, A. Bogdanov, and Y. Kivshar, "High-q quasi-bound states in the continuum in the far-infrared range," *Physical Review Letters*, vol. 123, no. 25, p. 253 901, 2019. DOI: 10.1103/PhysRevLett.123.253901.

[22] K.-H. Kim and I.-P. Kim, "Quasi-bound states in the continuum with high q-factors in metasurfaces of lower-index dielectrics supported by metallic substrates," *RSC Advances*, vol. 12, no. 4, pp. 1961–1967, 2022. DOI: 10.1039/D1RA07858E.

[23] Z. Huang, J. Wang, W. Jia, S. Zhang, and C. Zhou, "All-dielectric metasurfaces enabled by quasi-bic for high-q near-perfect light absorption," *Optics Letters*, vol. 50, no. 1, pp. 105–108, 2025. DOI: 10.1364/OL.541553.

[24] U. Kuhl, H. St"ockmann, and R. Weaver, "Experimental wave chaos in a microwave cavity," *Physical Review Letters*, vol. 94, no. 14, p. 144 101, 2005. DOI: 10.1103/PhysRevLett.94.144101.

[25] S. Wiggins, *Introduction to Applied Nonlinear Dynamical Systems and Chaos*. Springer, 2003.

[26] J. Guckenheimer and P. Holmes, *Nonlinear Oscillations, Dynamical Systems, and Bifurcations of Vector Fields* (Applied Mathematical Sciences). Springer, 2002, vol. 42.

[27] H.-J. Stockmann, *Quantum Chaos: An Introduction*. Cambridge University Press, 2000.

[28] A. Jafargholi, M. Safaei, R. Fleury, and R. Tafazolli, "Low-profile espar using metamaterial-inspired structure," *IEEE Open Journal of Antennas and Propagation*, 2024.

[29] W. Huang, S.-T. Cao, W. Zhang, S. Yin, and J. Han, "Analogy to debye model in metamaterials: Resonant frequency shifting due to coupling," *Optics and Laser Technology*, vol. 169, p. 109 545, 2024. DOI: 10.1016/j.optlastec.2023.109545.

[30] *Wlan channels and frequencies: 802.11 wi-fi standard*, 2025. [Online]. Available: https://www.rfwireless-world.com/terminology/wlan/wlan-channels-and-frequencies.

[31] J. W. Goodman, *Introduction to Fourier Optics*. Roberts and Company Publishers, 2005.

[32] E. Hecht, *Optics*, 5th. Pearson Education, 2016.

[33] M. Born and E. Wolf, *Principles of Optics: Electromagnetic Theory of Propagation, Interference and Diffraction of Light*, 7th. Cambridge University Press, 1999.

[34] G. Indiveri, B. Linares-Barranco, R. Legenstein, G. Deligeorgis, and T. Prodromakis, "Neuromorphic silicon neuron circuits," *Frontiers in neuroscience*, vol. 5, p. 73, 2011. DOI: 10.3389/fnins.2011.00073.

[35] E. Chicca, F. Stefanini, C. Bartolozzi, and G. Indiveri, "Neuromorphic computing: From materials to systems architecture," *Science*, vol. 345, no. 6197, pp. 1246–1250, 2014. DOI: 10.1126/science.1253722.

[36] J. Serra, *Image Analysis and Mathematical Morphology*. Academic Press, 1982.

[37] R. C. Gonzalez and R. E. Woods, *Digital Image Processing*. Prentice Hall, 2008.

[38] C. W. J. Beenakker, "Random-matrix theory of quantum transport," *Reviews of Modern Physics*, vol. 69, no. 3, pp. 731–808, 1997.

[39] E. Ott, *Chaos in Dynamical Systems*. Cambridge University Press, 2002.

7 List of Figures

List of Figures